



# **AALBORG UNIVERSITY**

## STUDENT REPORT

### Production and Deposition of Copper Clusters Using Magnetron Sputtering

**Supervisor:** Vladimir Popok and Muhammad Hanif

**Written by:**

Jonas Daugaard Hulstrøm

September, 2014



# Production and Deposition of Copper Clusters Using Magnetron Sputtering

Thesis by

Jonas Daugaard Hulstrøm

Aalborg University, Skjernvej 4A, DK-9220 Aalborg Øst

Supervised by

Vladimir Popok and Muhammad Hanif

Aalborg University, Skjernvej 4A, DK-9220 Aalborg Øst

## Abstract

The aim of the project was to construct and test a setup for producing size selected copper clusters using a magnetron sputtering source. The cluster deposition apparatus has been constructed and a series of experiments were performed to determine the deposition parameters for maximum cluster beam intensity. Different substrate materials were studied which was best suited for further deposition. At the end the cluster size selection was tested at different electrostatic quadropole mass spectrometer (QMS) voltages. Atomic force microscopy revealed that the cluster size increases with the QMS voltage, which is in agreement with the theoretical prediction ( $r \propto \sqrt[3]{U_{QP}}$ ).

**Concluded** September 12th 2014

**Number of pages:** 45 (53)

**Number of appendices:** 0

---

Jonas Daugaard Hulstrøm



# Resumé

---

Formålet med projektet beskrevet i dette speciale er at konstruere og teste et setup til at producere og størrelsesselektre metalclustre. Clustrene blev producerede ved hjælp af magnetron katodeforstøver og størrelsesselektionen blev udført ved hjælp af et electrostatisk quadropol massespektrometer (QMS). det benyttede metal var kobber.

Først gennemgås noget teori omkring clustre, startende med den spheriske cluster approksimation. stabiliteten af metalclustre vil herefter blive undersøgt via først opfyldningen af elektroniske orbitaler, hvor stabiliteten bestemmes af den elektroniske struktur der dannes af clusterkomponenternes valenselektroner. Efterhånden som cluster størrelsen stiger begynder stabiliteten i stedet at være styret af lukningen af geometriske skaller. Herefter beskrives flere metoder til at fremstille clustre, og der lægges vægt på magnetron katodeforstøvning. Denne type kilde fungerer ved at ioner af inert gas forstøver materiale fra kilden hvorimens de sekundære elektroner der bliver tilbageholdt af et magnetisk felt holder plasmaen vedlige. Efter dette bliver dannelse og styring af stråler af clustre, specielt ladede clustre, beskrevet. Herefter kommer en beskrivelse af hvordan clustre og overflader interagerer. Denne interaktion styres primært af den kinetiske energi per atom i clustren. De to hovedregimer er hård og blød landing der skelnes ud fra hvorvidt den kinetiske energi overstiger bindingenergien i clustren og dermed om en kollision kan give anledning til at clustren fraktureres.

I det næste kapittel bliver setuppet og nøglekomponenterne beskrevet. Først gives et overblik over setuppet og strålegangen beskrives. Herefter gives en beskrivelse af principperne bag vacuumsystemet samt turbomolekylære og lamel pumper. Herefter beskrives den magnetron katodeforstøver som benyttes i dette setup. Efter dette gives en beskrivelse af ionoptikken og QMS'et. Samt et overblik over hvordan denne type størrelsesselektion fungerer. Derpå gives en beskrivelse af principperne for atomart kraftmikroskopi med fokus på semikontakt metoden.

Så gives de eksperimentelle resultater for de tre udførte set eksperimenter. Først for de eksperimenter der blev udført for at justere setuppet samt at finde deponeringsparametrene. Derpå for det set der testede hvilket af tre substratmaterialer var best egnet til at deponere kobberclustrene på. Til slut blev størrelsesselektionen testet.

Det blev fundet at silicium var det bedste materiale at deponere på og at som forventet steg størrelsen på clustrene med QMS spændingen.

# Summary

---

The purpose of the project described in this thesis is to construct and test a setup for production and size selection of metal clusters. The cluster production was accomplished using a magnetron sputtering source and the size selection was performed using an electrostatic quadropole mass spectrometer (QMS). The clusters produced were made of copper.

First some theory regarding clusters will be described, starting from the spherical cluster approximation. The stability of metal clusters will then be examined through first the filling of electronic orbitals, where the stability is determined by the electronic structure formed by the valence electrons of the cluster constituents. As the cluster size increases the stability instead is governed by the closing of geometrical shells. Then several techniques for production of clusters are described with focus being on the magnetron sputtering source. This source functions by sputtering the target with ions of an inert gas while using the secondary electrons confined by a magnetic field to sustain the plasma. After this the formation and control of beams of clusters, in particular beams of charged clusters is described. Followed by a description of the interaction between clusters and a surface. This interaction is governed primarily by the kinetic energy of the cluster per constituent atom. The two main regimes are soft and hard landing which are distinguished by whether the kinetic energy is above the binding energy of the cluster and thereby whether the impact can fracture the cluster.

In the next chapter the setup and the key components are described. First an overview of the setup and the beam path is given. This is followed by a description of the working principles of the vacuum system as well as turbomolecular and rotary vane pumps. Then a description of the magnetron source used in the setup is given. Following this a description of the ion optics and in particular the QMS. As well as a description of the working principles of this type of mass selection. Then a description of the working principles of atomic force microscopy and in particular the semi-contact mode was given.

Then the experimental results are given for the three sets of experiments. First the experiments performed to determine the deposition parameters and ensure the alignment of the setup. Secondly the experiments done to determine which substrate material to utilize for cluster deposition. And lastly the experiments performed to test the size selection of the clusters.

It was found that silicon was the best of the three tested materials to deposit clusters. And that as expected an increasing QMS voltage gave increasing cluster sizes.

# Contents

---

<b>Resumé</b>	<b>v</b>
<b>Summary</b>	<b>vi</b>
<b>1 Introduction</b>	<b>1</b>
<b>2 Clusters</b>	<b>2</b>
2.1 Clusters and Spherical Approximation . . . . .	2
2.2 Metal Clusters . . . . .	3
2.2.1 3D Harmonic Potential . . . . .	5
2.2.2 Square Well Potential . . . . .	5
2.2.3 Woods-Saxon Potential . . . . .	5
2.2.4 Geometrical shells . . . . .	7
2.3 Cluster Formation . . . . .	9
2.3.1 Effusion and Gas Aggregation Sources . . . . .	10
2.3.2 Seeded Supersonic Nozzle Source . . . . .	10
2.3.3 Laser Vaporization . . . . .	11
2.3.4 Magnetron Sputtering . . . . .	11
2.4 Cluster Beam Formation . . . . .	15
2.4.1 Nozzles and Skimmers . . . . .	15
2.4.2 Ion Optics . . . . .	16
2.4.3 Mass Filters . . . . .	17
2.5 Cluster-Surface Interaction . . . . .	17
<b>3 Experimental Setup</b>	<b>22</b>
3.1 Vacuum Systems . . . . .	23
3.2 Magnetron Source . . . . .	24
3.3 Ion Optics and Quadropole Mass Spectrometer . . . . .	25
3.4 Characterization of deposited clusters by AFM . . . . .	27
<b>4 Optimization of the Magnetron Cluster Source</b>	<b>30</b>
4.1 Optimizing lens and deflector voltages . . . . .	30
4.2 Testing of the Quadropole Mass Spectrometer . . . . .	31
4.2.1 Cluster Deposition on Differnt Substrates . . . . .	32
4.2.2 Size Selection . . . . .	37
<b>5 Conclusion</b>	<b>42</b>

**Bibliography**

**43**

# Introduction 1

---

A cluster is an aggregate consisting of a countable number of atoms (from 2 to about  $10^7$ ). It can contain either one or more atomic species (homo- or heteroclusters). Clusters are further categorized by the types(s) of atom(s) e.g. metal, semiconductor, rare gas, etc. Clusters are studied both in the gas phase as well as deposited on surfaces and embedded in materials [1],[2],[3],[4].

Clusters straddle the boundary between atomic scale and bulk materials. However it is not only the fact that clusters can range in size from the atomic to the microcrystalline level. They also have properties that are unique to the nanoparticle domain such as the size dependent electronic structure. They can follow geometric structures that are not seen in bulk materials such as the fivefold symmetry found in metal clusters or the buckyball structure of a carbon cluster with 60 atoms. Due to quantum confinement clusters of non-magnetic materials might become magnetic, semiconducting materials might have metallic properties, and metallic systems become semiconducting or dielectric [5],[6]. Clusters can also be seen as a bridge between nuclear and condensed matter physics in that clusters exhibit the same tendency towards a certain number of constituents, magic numbers, as nuclei with an equal number of proton and neutrons do. Also analogous to nuclei is the way a cluster fragments. The products of fragmentation tends toward these magic numbers much the same way products of nuclear fission do. In the field of chemistry cluster production techniques have been used to study organometallic compounds in the gas phase and thus study the interaction without accounting for a solvent [7].

In this thesis first a description of the theory regarding clusters and in particular metal clusters as well as the methods for producing and depositing them will be described. After that the setup will be described, including the vacuum system, the cluster source, the ion optics, and the basic operating principle of atomic force microscopy (AFM). Then the sample preparation and experimental results are presented. First the optimization of the deposition parameters. Second, deposition on different substrates and lastly a set of experiments will be described regarding size selection of the clusters.

# Clusters 2

---

## 2.1 Clusters and Spherical Approximation

Close packing of atoms in clusters leads to the high amount of surface atoms. This means that they have some properties that closely resemble bulk surfaces. In order to describe cluster properties as a function of size some approximations are developed.

The spherical cluster approximation (SCA) represents a cluster containing  $N$  atoms as a sphere. This approximation gets better the larger a cluster becomes and allows for an equation for the number of surface atoms in the limit of a large cluster. In this approximation the volume of the cluster ( $V_c$ ) is:

$$V_c = N \cdot V_a, \quad (2.1)$$

where  $N$  is the number of atoms in the cluster and  $V_a$  is the volume of a single atom. This does not take into account packing ratios, however what is sought is the scaling relationships. This then allows for finding the relationship between the cluster and atomic radii ( $R_c$  and  $R_a$  respectively):

$$\frac{4}{3}R_c^3\pi = N\frac{4}{3}R_a^3\pi \quad (2.2)$$

$$R_c = N^{\frac{1}{3}}R_a \quad (2.3)$$

which again means that the surface areas of the cluster ( $S_c$ ) and atom ( $S_a$ ) are related as

$$S_c = N^{\frac{2}{3}}S_a. \quad (2.4)$$

Then the number of surface atoms ( $N_s$ ) in the large cluster limit can be found as the fraction between cluster surface area and the atomic cross-sectional area

$$N_s = \frac{4\pi R_c^2 N^{\frac{2}{3}}}{\pi R_a^2} = 4N^{\frac{2}{3}} \quad (2.5)$$

and then the fraction of surface atoms will be  $F_s = 4N^{-\frac{1}{3}}$ , see fig. 2.1 for a plot of this function, which means that a relatively small cluster has the majority of its atoms on the surface. For example, one with 75 atoms would have about 80% of them on the surface. This makes clusters very attractive for catalytic applications because only the surface atoms are chemically active. It means that by using clusters one can provide maximum efficiency with minimal material [1].

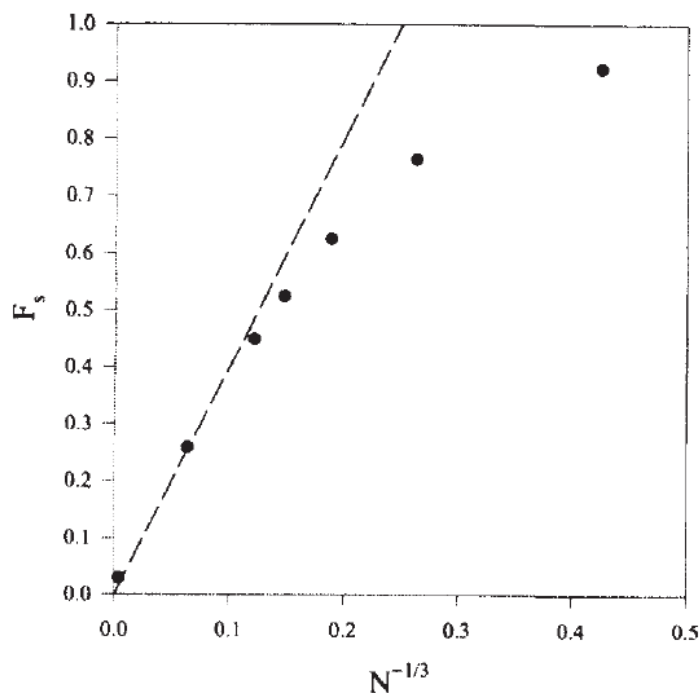


*Figure 2.1.* A plot of fraction of surface atoms versus  $N^{-1/3}$  for an icosahedral cluster (dots) and the spherical cluster approximation (dashed line) [1].

## 2.2 Metal Clusters

In order to describe metal clusters several different models can be used. One possible test for a model is the so-called magic numbers that are peaks in the abundance spectra at certain numbers of atoms, see fig. 2.2 [1]. These have been found experimentally and represent states that are more electronically stable. This stability is caused by the filling of electronic shells by the delocalized valence electrons of the constituent atoms, and the cluster could as such be regarded as a 'superatom'. The magic numbers are the numbers of atoms required to completely fill a given electronic shell. Assuming that every atom contribute with one valence electron, as in the case of alkali metals [8]. In fig. 2.2 an abundance spectrum for sodium clusters is shown and the first magic numbers have been marked.

The spherical Jellium model describes a metal cluster as a uniform positively charged sphere containing an electron gas. One can then solve the Schrödinger equation for an electron confined to the sphere and subject to the mean field potential from the ionic cores. The position of the ionic cores is neglected which is valid as long as the valence electrons are weakly bound and the ionic background easily responds to perturbations. This is true for both alkali and coinage metals (copper, silver, and gold). The Jellium model only applies when the cluster is molten however the melting point is dependent on the size of the cluster and as such small cluster might indeed be molten under experimental conditions. Due to the quantum mechanical nature of the Jellium model and the boundary conditions imposed by the potential, the electronic energy levels will be quantized. The potential can be found either empirically or

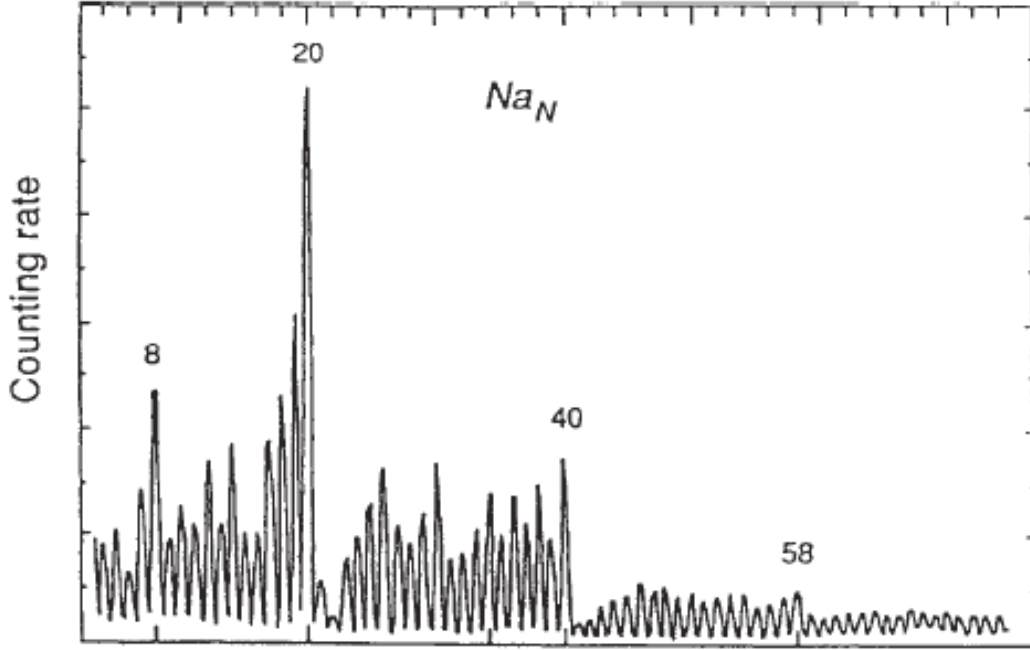


Figure 2.2. Cluster abundance versus cluster size for sodium clusters [1].

using either Hartree-Fock molecular orbital calculations or Density Functional Theory (DFT).

Empirical Jellium models have been developed based on assumed effective single particle potentials and solving the Schrödinger equation for a particle inside a sphere constrained to move under an attractive central potential. Due to the potential being spherical in nature and that it acts from the centre of the cluster, the Jellium orbitals ( $\Psi$ ) are separable into radial (R) and angular (Y) parts:

$$\Psi(r, \theta, \phi)_{n,l,m_l} = R(r)_n Y(\theta, \phi)_{l,m_l} \quad (2.6)$$

where by analogy to atoms,  $n, l, m_l$  are, respectively, the principal, angular momentum, and magnetic quantum numbers. They can have values as follows:

$$n = 1, 2, 3... \quad (2.7)$$

$$l = 0, 1, 2... \quad (2.8)$$

$$m_l = -l..0, ..l \quad (2.9)$$

These Jellium orbitals are labelled like atomic orbitals with  $n = 1, l = m_l = 0$  being a 1S Jellium orbital. Magic numbers arise due to the filling of these Jellium levels. It is important to note that the principal Jellium quantum number is different from the atomic principal quantum ( $n_{at}$ ) number by 1 that is  $n = n_{at} - 1$ . The energy of the levels increase, like it is the case with atoms, with increasing principal quantum number and increasing angular momentum quantum number, while the  $(2n + 1)$  orbitals with the same  $m_l$  are degenerate. However the exact ordering of the orbitals depends on the radial potential. There are several potentials that can be used to describe a metal cluster.

### 2.2.1 3D Harmonic Potential

The 3D harmonic potential is the simplest of the potentials used in the spherical Jellium model. This is the expected potential for electrons moving in a field due to a smeared out positive charge when there is assumed no interaction between the electrons [9]:

$$U(r) = \frac{1}{2}\omega_0^2 m_e r^2, \quad (2.10)$$

where  $r$  is the radial position,  $m_e$  is the mass of the electron, and  $\omega$  is the fundamental frequency. All orbitals with the same value of  $2n + l$ , are degenerate i.e. have the same energy. This leads to the characterization of the energies with just one quantum number  $v = 2n + l - 2$ . The ordering of the orbitals are then as follows:

$$1s(v=0) < 1p(v=1) < 1d, 2s(v=2) < 1f, 2p(v=3) < 1g, 2d, 3s(v=4) \quad (2.11)$$

This leads to the magic numbers being predicted as 2, 8, 20, 40, 70 etc. and while peaks in intensity has been observed at 8, 20, and 40 this potential does not account for the peak in intensity at 58 atoms, see fig. 2.2, and is therefore too simple for describing the electronic structure of a cluster.

### 2.2.2 Square Well Potential

In the square well potential the potential is assumed to be constant within the cluster and zero at the radius ( $r_0$ ) of the cluster. This potential comes from models considering the exchange-correlation hole that exists around each electron i.e. the tendency for electrons to avoid each other due to the Pauli exclusion principle and the Coulomb repulsion. For a square well potential there is zero probability of finding the electron at a distance  $r \geq r_0$ . This leads the wave functions to be spherical Bessel functions and to the following ordering of the orbitals:

$$1s < 1p < 1d < 2s < 2p < 1g \quad (2.12)$$

The predicted magic numbers for the square well potential are: 2, 8, 18, 20, 34, 40, 58 etc. This does unlike the harmonic potential predicts the intensity peak at 58, however it also predicts one at 34 which has not been found experimentally Thus, that this potential is better than the 3d harmonic potential but is still not satisfactory.

### 2.2.3 Woods-Saxon Potential

The Woods-Saxon Potential is the most widely used radial potential [1], which was originally developed to describe atomic nuclei. It has the following mathematical form:

$$U(r) = \frac{-U_0}{e^{r-r_0/\sigma} + 1}, \quad (2.13)$$

where  $U_0$  is given as the sum of the Fermi energy and the work function for the bulk metal.  $r_0$  is the effective radius of the cluster given as  $r_0 = N^{\frac{1}{3}} r_{ws}$  where  $r_{ws}$  is the Wigner-Seitz radius,  $r$  is the radial position, and  $\sigma$  is a constant scaling factor of 1.5 Bohr. This gives, as can be seen in fig. 2.3, a potential that is like a square well potential with rounded sides and therefore in between the two former potentials. The ordering of the orbitals is as follows:

$$1s < 1p < 1d < 2s < 1f < 2p < 1g \quad (2.14)$$

This means that the potential has the same predicted magic numbers as the square well potential for  $N$  less than 68 atoms. Above this number it predicts the magic numbers more accurately than the two above mentioned potentials.

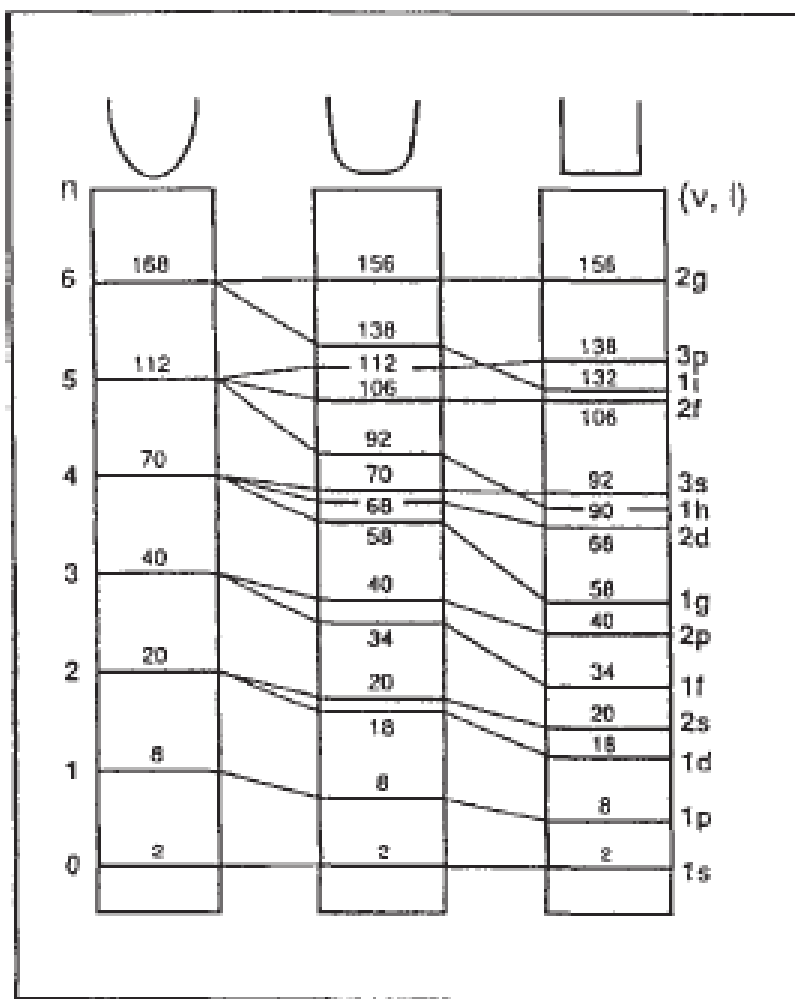


**Figure 2.3.** Comparison of energy levels and predictions of magic numbers using 3 different potentials. On the left there is the 3D harmonic potential, in the middle there is the Woods-Saxon potential, and on the right there is the square well potential [1].

The above-mentioned potentials can be seen in fig. 2.3 along with their predicted magic numbers. The closing of electronic orbitals predict the magic numbers for clusters with a few tenths of atoms well, however they fail to explain larger clusters. For clusters of up to 2000 atoms what determines the stability is the filling of the electronic shells which are groups of jellium orbitals that are approximately degenerate. The condition for approximate degeneracy is that the value  $(3n + l)$  is the same for the respective electronic levels. An analogy can be made to the hydrogen atom where all orbitals with the same values  $n + l$  are degenerate. As the cluster size increases a longer order oscillation in the abundance spectrum becomes apparent which can be understood as the merging together of the electronic shells into band like supershells.

### 2.2.4 Geometrical shells

For relatively large clusters geometrical packing of atoms becomes an important factor. There is typically one central-positioned atom and the others makes shells around it. For Sodium and the other alkali metals the drops in intensity, caused by increased stability and therefore a lower ionization cross-section, correspond to shells that are concentric polyhedra with twelve vertices e.g. icosahedrons. The smallest icosahedron-shaped cluster consists of 13 atoms: 1 in the centre and 12 making a shell around it. An icosahedral cluster with 561 atoms can be seen in fig. 2.4. For clusters based on twelve vertex polyhedra the magic numbers ( $N^*$ ) as a function of the number of filled shells ( $K$ ) are:

$$N^*(K) = \frac{1}{3} (10K^3 - 15K^2 + 11K - 3), \quad (2.15)$$

which will lead to the following magic numbers:

$$N_* = 13, 55, 147, 309, 561, 923, 1415...$$

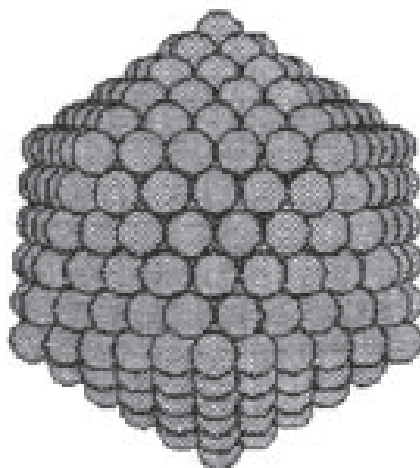


*Figure 2.4.* An illustration of an icosahedral cluster with 561 atoms [1].

The change from electronic to geometric governance of the stability is dependent on several factors such as electronic density of states, electronic configuration of the atoms, temperature of the cluster, and the cluster melting point. It is assumed that under experimental conditions that the atomic nuclei of a small cluster are mobile and it as such can be regarded as a spherical molten drop. The quantization of the movement of the electrons leads to a jellium structure. As the size of the cluster increases the Jellium levels bunch together until first shells then supershells and lastly semi continuous bands are formed, when the level spacing is  $\Delta \ll kt$ . It can be assumed that once the level spacing,  $\Delta$ , is small compared to  $kt$  electronic shell filling will no longer govern the stability of the cluster as there will be no preference for any specific electron counts.

If the cluster has a temperature that is under the melting point the clusters will grow as

solid like nanocrystallites. This means that crystalline growth effects govern structure and stability, and that the shell structure will be geometric.

If the cluster is molten,  $T > T_m$ , then it will resemble a liquid-like spherical drop and therefore all geometric effects will disappear as there is no longer a crystalline structure. For some metals such as aluminium and sodium this melting also marks a transition to electronic shell structure. It is however important to remark that  $T_m$  is dependent on the size of the cluster.

The size dependence of cluster melting is not simple as the energy and entropy differences between the liquid and solid states exhibit pronounced maxima at nuclearities corresponding to geometrical shell and sub shell closings. This causes fluctuations in the melting temperature as seen in fig. 2.5. Which show the importance of geometric shell closings with regard to the melting temperature [10].

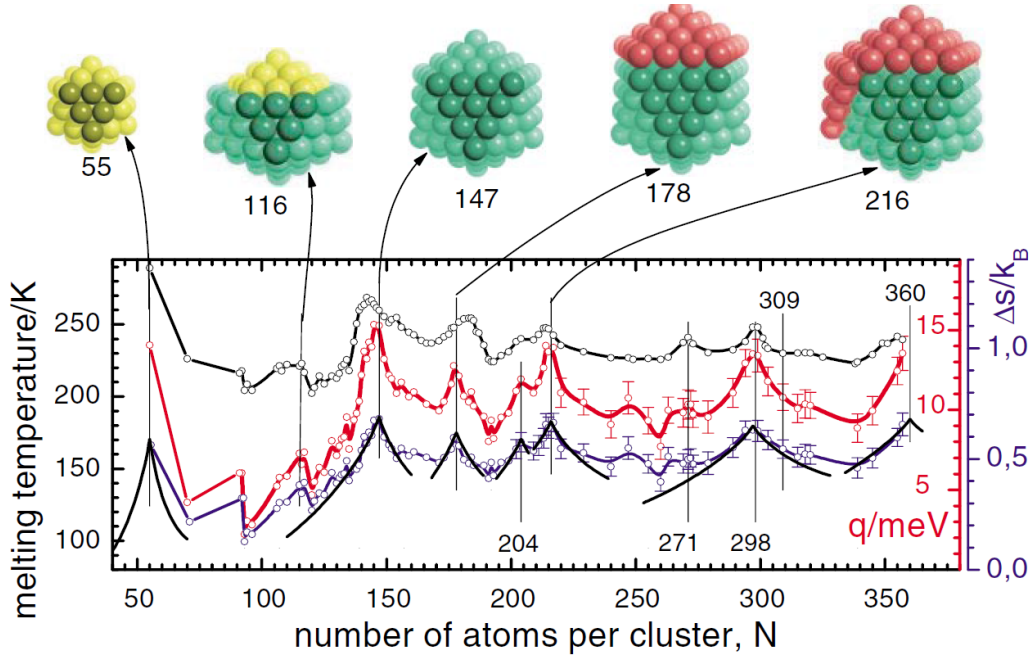


**Figure 2.5.** Upper panel suggested cluster structures with the first layer of atoms in yellow the second in green and the third in red. the black line represents the melting temperature, the blue the change in entropy per atom and the red the latent heat of fusion per atom. The solid black lines partially overlapping with the blue line give a calculated change of entropy [10].

Since icosahedral and decahedral geometry have fivefold symmetry axes they are non-crystalline in their packing. However since bulk metals are crystalline a shift from one geometry to the other has to occur at some point. For small and medium sized clusters the high surface to volume ratio means that the surface energy is unfavourable to crystalline packing and can be reduced by adopting highly coordinated structures like deca- or icosahedral structures.

As the cluster grows the surface energy becomes less important as the elastic strain, a bulk effect, grows. The balance between the surface and bulk effects depend on the surface to bulk ratio which goes as  $N^{-\frac{1}{3}}$ . There must therefore be a certain nuclearity at which a change occurs from surface to bulk dependence of the structure [1], [11].

When a metal cluster adopts bulk-like structure it will have the packing of the bulk for the coinage metals this means fcc structure. However it is still favourable for the cluster to have as low surface energy as possible. Therefore, it will adopt a polyhedral structure that minimizes the surface area. A basic shape is an octahedron and while this is the form taken by aluminium clusters, for most clusters the surface area is too high. This can be resolved by truncating the octahedron with a cube, resulting in a cuboctahedron. This structure can be seen in fig. 2.6. The total number of atoms in a cuboctahedral cluster with  $K$  atoms along the side of a face is:

$$N = \frac{1}{3} (10K^3 - 15K^2 + 11K - 3) \quad (2.16)$$

which is the same as for the icosahedron. It has a single central atom regardless of size and can be considered to consists of  $K$  successive shells each covering the last and each containing  $10K^2 + 2$  atoms[9].

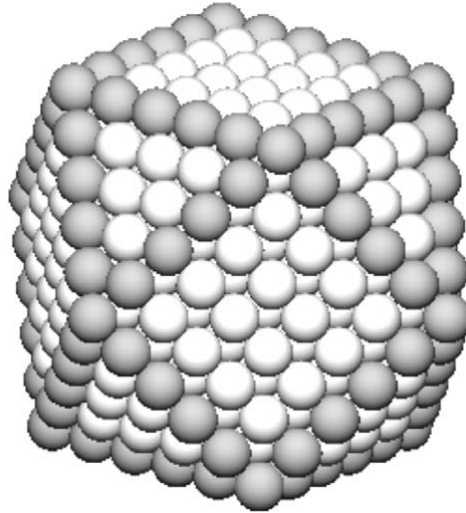


**Figure 2.6.** An illustration of a cuboctahedral cluster with 561 atoms. The edge and face atoms have been given different shades to make the shape clearer [9].

## 2.3 Cluster Formation

Formation of clusters from the gas phase consists of the following stages: Vaporization, nucleation, growth, coalescence, and evaporation. The chances of nucleation of a cluster at thermal equilibrium is very small. Therefore, cluster production requires a thermal non-equilibrium which can be implemented using one of the cluster sources described below. If the thermal energy of the monomer species is less than the binding energy of dimer then a

triple collision can cause the dimer to be formed:



where the third atom has (A on the right-hand side) removes the excess of energy released due to the dimer formation. Often a carrier gas is injected into the chamber to make the nucleation more efficient i.e. the third atoms in the scheme can be of other species than those composing clusters. The dimer acts a nucleation point for further growth, which in the beginning consists of adding single atoms to the cluster but later can be coalescence of smaller clusters into large ones. In the growth region the cluster are normally hot as the addition of more atoms is an exothermic process. This causes growth and decay to be competing processes and it is therefore often necessary to cool the nucleation chamber. This cooling can be done by collisional cooling where the cluster loses energy by colliding with other atoms.



where B can be a single atom of the same species as A or as is more common a cold carrier gas. E is the internal energy of the cluster and  $\epsilon$  is the kinetic energy of the atom. Clusters can also lower their internal energy by evaporative cooling where one or more atoms are ejected from the cluster and cooling the cluster by the endothermic desorption process. More details about providing the thermal non-equilibrium conditions are given below in the description of a few different types of cluster sources. The focus is given on magnetron sputtering as the main method used in this work [12], [13].

### 2.3.1 Effusion and Gas Aggregation Sources

The simplest method for production of clusters is an effusion source where a liquid or solid is vaporised in an oven. Since the vapour is kept in equilibrium with the oven only a small fraction of clusters are produced and the intensity of falls exponentially with cluster size. The beam of clusters and atoms is formed when the vapour is forced through a nozzle into a lower pressure region. An improvement over this is the aggregation source where the vapour is mixed with flow of cold inert gas. This causes supersaturation of the vapour which leads to condensation of clusters. Cluster have been made from both alkali and noble metals using this technique. Clusters of over 20000 atoms have been made using this process [14], [12].

### 2.3.2 Seeded Supersonic Nozzle Source

The supersonic seeded nozzle source works on the principle of adiabatic expansion of a gas into a vacuum. The source can make clusters of relative low melting point metals. The metal is vaporised and seeded into an inert carrier gas. The carrier gas is often at several atmospheres of pressure and the metal vapour pressure is in the range of 10-100mbar. This mixture is expanded into vacuum through a small nozzle such that the expansion of the mixture creates a supersonic beam. This expansion rapidly cools the mixture forcing it to be supersaturated with metal vapour which causes clusters to condense. The clusters continue to grow until the saturation of gas becomes too low. These sources produce intense continuous or pulsed cluster beams with narrow velocity distributions and clusters that can range in size from tens to thousands of atoms [14], [12].

### 2.3.3 Laser Vaporization

The previous sources needed metals that could be vaporized in an oven. Laser vaporization produces a pulsed stream of small clusters made from any metal, usually those with a high melting point that cannot be evaporated with simple heating. The source vaporizes the metal by ablating a small rod of the relevant metal using a pulsed laser. The metal vapour is entrained in a pulse of cold carrier gas which cools the metal and causes cluster formation. The mixture is then ejected from a nozzle which causes adiabatic cooling which in turn means that the clusters are cold (some were found to be below 100K). The cluster sizes range from several to several hundred atoms. The laser can also be replaced with an arc discharge which has the added benefit of ionizing approximately 10% of the clusters which in turn makes electrostatic manipulation of the cluster beam easier [14], [12].

### 2.3.4 Magnetron Sputtering

In a sputtering process an inert gas, e.g. argon, is ionized by a glow discharge forming a plasma. The gas ions are accelerated by the same potential that caused the discharge and impact a target consisting of the material to be sputtered. This impact causes some of the target material to be ejected. Along with the material so called secondary electrons are also emitted and accelerated away from the target by the potential. These electrons further contribute to the plasma ionization. In order to keep the sputtering process going new sputtering gas is continuously released in the vicinity of the target. Magnetrons use a magnetic field to keep the motion of the secondary electrons in the vicinity of the target. This confinement increases the chances that an ionizing electron atom collision occurs. This leads to a denser plasma and therefore a higher rate of sputtering. An illustration of a planar magnetron can be seen in fig. 2.7 [15].

A glow discharge plasma can be defined as a region of gas which has a relatively low

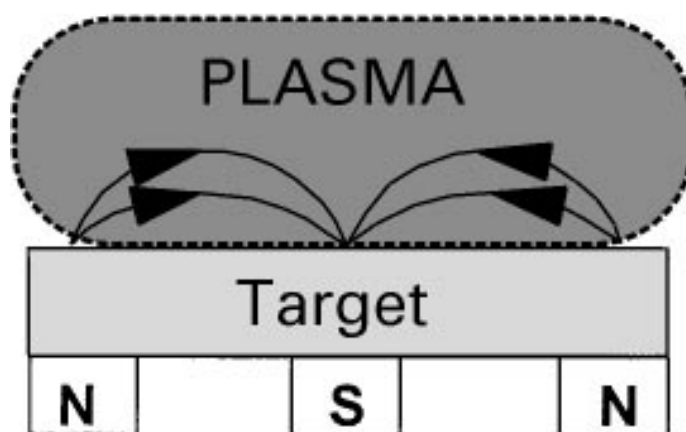


*Figure 2.7.* A schematic of the plasma confinement in a planar magnetron [15].

temperature and a high degree of ionization sustained by energetic electrons. Such a plasma

is characterised by the degree of ionization:

$$\alpha = \frac{N_e}{N_i + N_a}, \quad (2.19)$$

where  $N_e$  is the density of electron,  $N_i = N_e$  is the density of ions, and  $N_a$  is the gas density. The plasma is also characterised by the electron energy distribution which can be approximated by an electron temperature ( $T_e$ ). Due to long range Coulomb interactions the plasma has a tendency towards collective behaviour. In order for Coulomb collisions to be dominant the degree of ionization has to be:

$$\alpha \gg 1.7 \cdot 10^{16} \sigma_{eA} T_e^2, \quad (2.20)$$

where  $\sigma_{eA}$  is the electron-atom collision cross section. If the angular frequency of the plasma ( $\omega_p = 56.4 N_e^{\frac{1}{2}}$ ) is much larger than the electron-atom collision frequency then electrostatic waves can be expected to form. The distance over which significant departures from neutrality can occur is described by the Debye length ( $\lambda_D = 7430 \frac{T_e}{N_e^{\frac{1}{2}}}$ ). Magnetron plasmas have a higher degree of ionization and a much higher degree of collective behaviour than conventional diode sputtering devices.

Despite the importance of the collective behaviour the motion of a single particle pro-

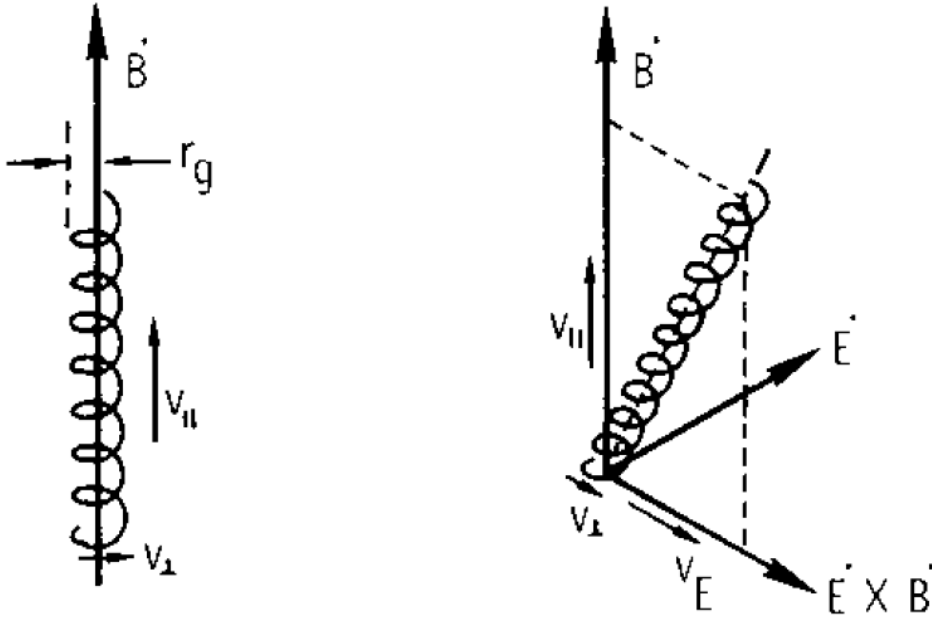


**Figure 2.8.** Trajectory of an electron moving with a speed  $v_{||}$  parallel to a magnetic field ( $\vec{B}$ ), orbiting the magnetic field lines at a radius  $r_g$  (left). Trajectory of an electron moving in perpendicular magnetic and electric fields ( $\vec{E}$ ), This causes a drift with velocity  $v_E$  (right) [16].

vides useful insight into the behaviour of magnetron plasmas. An electron, the only particles significantly influenced by the magnetic field in the magnetron, in a uniform magnetic field

( $B$ ) will drift along the field lines with a speed ( $v_{\parallel}$ ) that is unaffected by the field. It will orbit the lines at a radius of:

$$r_g = 3.37 \cdot 10^{-6} \frac{W_{\perp}^{\frac{1}{2}}}{B}. \quad (2.21)$$

Where  $W_{\perp}$  is the energy associated with the perpendicular motion of the electron relative to the field. The frequency of the orbit will be  $\omega_c = 1.76 \cdot 10^{11} B$ . When there is a component of the electric field ( $E_{\perp}$ ) perpendicular to the magnetic field ( $\vec{B}$ ), a drift with a speed of  $v_e = \frac{E_{\perp}}{B}$  will develop in a direction perpendicular to both. This is the  $\vec{E} \times \vec{B}$  drift, see fig. 2.8. This leads to a cycloidal motion with a radius  $r_g(v_e)$  which is the radius obtained by setting  $W_{\perp} = \frac{1}{2} m_e v_e^2$  with  $m_e$  being the mass of the electron [16].

This leads to a high ionization efficiency and therefore the possibility for the plasma to be sustained at much lower pressures than conventional sputtering. In a planar magnetron the target is circular and placed on top of an array of permanent magnets with one magnetic pole at the centre and the other at the edge. This causes the field lines to form arcs from the edge to the centre which along with the electrical field applied perpendicular to the surface causes the plasma to be confined near the target in a torus shape as seen in fig. 2.10 leading to a non-uniform erosion of the target as seen in fig. 2.9. The sputtering yield is linearly dependent on the ion energy and can be found as:

$$S \propto (W_{ion} - W_{thres}) \quad (2.22)$$

Where  $W_{ion}$  is the energy of the ion and  $W_{thres}$  is a threshold energy that can be found as:

$$W_{thres} = 8U_s(M_1/M_2)^{2/5} \quad (2.23)$$

where  $U_s$  is the surface potential barrier and  $M_1$  and  $M_2$  are the mass numbers of the ion and the target respectively. In order for the electrons to be the only particles significantly influenced by the magnetic field, the strength of the field is adjusted to between 50 and 200 mT [17]. In order to fully understand the process of magnetron sputtering one must realise that



**Figure 2.9.** A copper target nonuniformly eroded by the magnetron sputtering process.

the motion of a single electron cannot truly describe the way the plasma behaves collectively with each particle influencing the others. This causes the conduction to be primarily Bohm

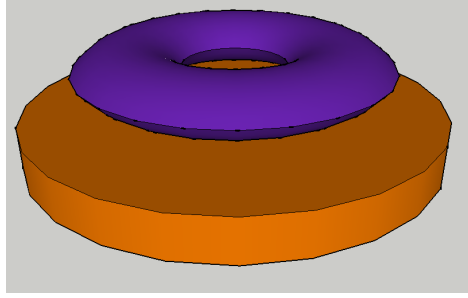


*Figure 2.10.* A schematic illustration of the plasma above the target.

diffusion rather than the classical collision dominated electron conduction across field lines. This diffusion is characterised by collective turbulent motion of the electrons. This means that the secondary electrons do not as one would expect move in cycloidal motions hopping along the  $\vec{E} \times \vec{B}$  drift path. But rather move in a turbulent, buffeted, and attenuated drift as the secondary electrons rapidly lose their energy to sustain the electron temperature of the plasma [18].

According to classical fluid theory Ions and electrons colliding with stationary neutral background atoms perpendicular to a magnetic field would have a mobility of:

$$\mu_{\perp}^s = \frac{\mu^s}{1 + (\omega_{cs}/\nu_s)} \quad (2.24)$$

Where s denotes the species, either ion or electron,  $\mu^s$  is the mobility in absence of a magnetic field,  $\omega_{cs}$  is the cyclotron frequency, and  $\nu_s$  is the mean frequency of collisions with neutral species. For the constant of diffusion the picture is much the same:

$$D_{\perp}^s = \frac{D^s}{1 + (\omega_{cs}/\nu_s)}, \quad (2.25)$$

where  $D^s$  is the diffusion constant in absence of a magnetic field. Under normal operating conditions for a magnetron the denominators are large for electrons thus the electron transport coefficients across the magnetic field are severely reduced. On the other hand the transport coefficients for ions are almost unchanged by the presence of a magnetic field. While electrons are more mobile parallel to the magnetic field, ions are often the most mobile perpendicular the field and thus they can leave the discharge more rapidly [19].

When a magnetron source is used for cluster production it is often used in combination with a gas aggregation source. That is the material sputtered from the target, along with a carrier gas flows through a cooled tube and this allows for both the already formed clusters to grow and for the single atoms to begin aggregating into clusters. The path length in the tube influences both the size of the clusters and the intensity of the beam [20]. From 20 to 80 % of the clusters produced in a magnetron source are charged, depending on the cluster species, which is important for the later control of the cluster beam [12].

## 2.4 Cluster Beam Formation

To use the produced clusters for any research or industrial application it is important to be able to control their parameters. Therefore, the clusters are typically collimated into beams by expansion through a nozzle and use of skimmers. Ions optics becomes an essential part of a cluster apparatus to be able to steer the beams. And finally different mass-selection methods can be applied in order to obtain clusters of desirable sizes. All these stages will be briefly over-viewed below.

### 2.4.1 Nozzles and Skimmers

For supersonic jet sources the geometry of the nozzle plays an important role and axially symmetrical beams are produced using nozzle geometries like those shown in fig. 2.11. The sonic nozzle is characterised by a hole in a wall much thinner than the diameter. The purpose of this design is to push the expansion to the limit, however several problems occur as the expansion occurs rapidly and the number of collisions is also low. This severely limits the growth of clusters. The overall effect of the nozzle diameter is that cluster abundance and size will increase with increasing nozzle cross section and pressure, and will decrease with increasing temperature. For conical nozzles it has been shown that the beam profile will follow the shape of the cone, with narrower angles giving high forward intensities. Compared to sonic nozzles conical nozzles have been shown to give about an order of magnitude more forward flow. It has also been shown that constraining the beam will allow for more cluster collisions and thus larger clusters [21].

Downstream from the nozzle a skimmer is placed. The purpose of this skimmer is to

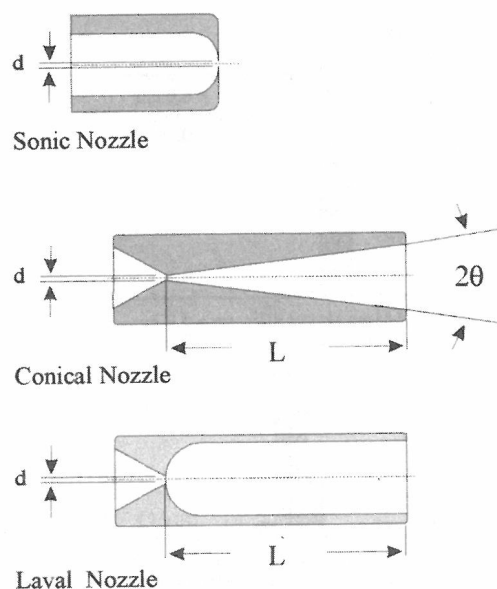


**Figure 2.11.** Schematic cross section of several nozzles [21].

extract only the isentropic centreline of the flow and thus create a more collimated beam. A skimmer is typically cone shaped with an aperture at the end of the cone, see fig. 2.12 [22].

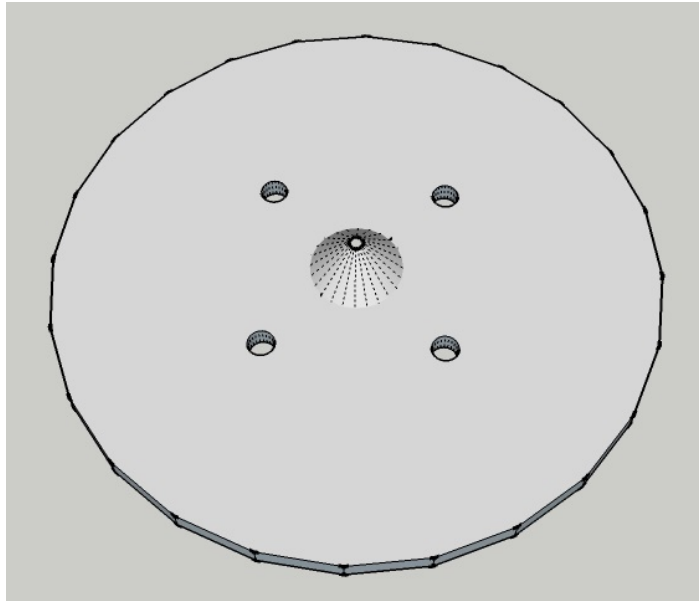


*Figure 2.12.* Schematic drawing of a skimmer.

### 2.4.2 Ion Optics

In order to get a better focused beam, ion optics can be used to influence the charged clusters in the beam. Many cluster sources produce predominantly neutral clusters. Thus, to apply ion optics the clusters need to be ionized which can be done using electron impacts, electric discharges or intensive light beams (lasers). Some cluster sources (for example, laser vaporisation or magnetron sputtering) produce a significant fraction of charged clusters. Hence, ion optics extracts these clusters from the beam. One way of focusing the charged clusters of a particular polarity is to use an Einzel lens. These consists of three concentric tubes (or rings) following each other. The edge parts are grounded and the middle one is a retarding electrode see fig. 2.13. The tubes do not necessarily have the same diameter or be very long, some are more like diaphragms than actual tubes. In the lens the ions have their kinetic energy ( $K_0$ ) reduced to a few percent of the one they entered with. When the ions leave the lens they are again accelerated. This decelerating and accelerating process causes the ions to be affected by focusing forces i.e. forces towards the optical axis in the middle of the lens and defocusing forces at the edges. The focusing forces are more effective since the ions are slower in the centre of the lens. If one changes the polarity of the middle tube the lens would be an accelerating lens for the same type of ions. this would also be a focusing lens as the focusing forces would then be at the edge where the ions would be slower [23].

For control of the direction of the focused beam of charged clusters one can use electrostatic deflectors which are simply two parallel plates with a difference in potential between them. A charged beam passing through the gap between them will experience an electric field and be deflected [23].

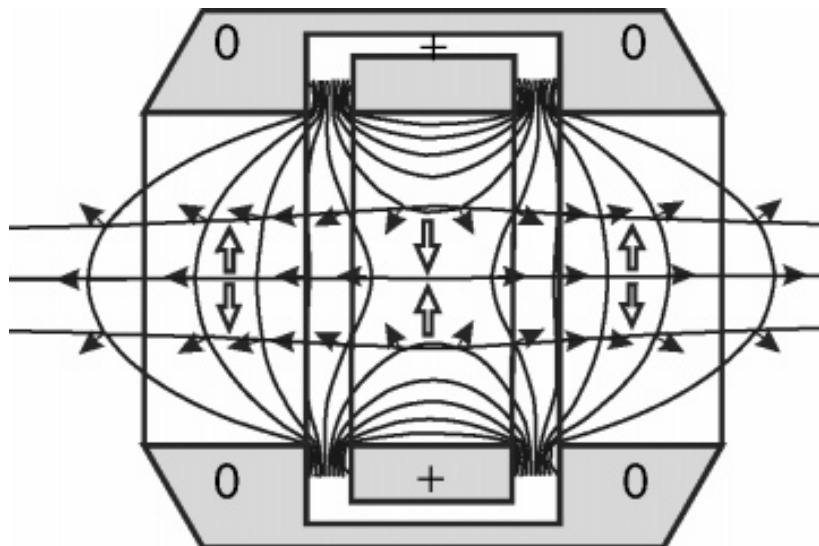


*Figure 2.13.* A figure showing a retarding Einzel lens (middle) for positive ions [23].

### 2.4.3 Mass Filters

There are several methods for size selecting clusters such as the Wien filter and the time of flight mass spectrometer more about these methods can be found in [24]. In this thesis an electrostatic quadrupole mass spectrometer was used. In these ions of a certain mass to charge ratio are deflected 90 degrees by the field generated by the poles which have the same voltage applied on each diagonal with the diagonals having opposite polarity to each other [20]. A further description will be given in section 3.3

## 2.5 Cluster-Surface Interaction

Clusters are very often used for various practical applications. One can bombard the surfaces to modify them on the nano scale or one can deposit clusters on the surface and utilize their specific properties. In both cases a knowledge about cluster-surface interaction is required. When describing the interaction of a beam of clusters with a surface the energy of the collision is important and therefore cluster beam regimes are split into two categories low energy deposition and high energy interaction.

While there is no precise boundary between the two cases the interaction can be considered low energy if the kinetic energy per atom is below the binding energy of the cluster and an impact would therefore not result in cluster fragmentation. This regime is called soft landing and while the composition of the cluster is preserved the structure may be distorted see fig. 2.14a. Soft landing can be used for many different applications were supported nanoparticles or their arrays are used. The main problem with clusters deposited in the soft landing regime is their high diffusive mobility which can cause the clusters to aggregate into islands or coalesce into large particles.

In the simplest regime of low energy impact the chance of a cluster diffusing more than a

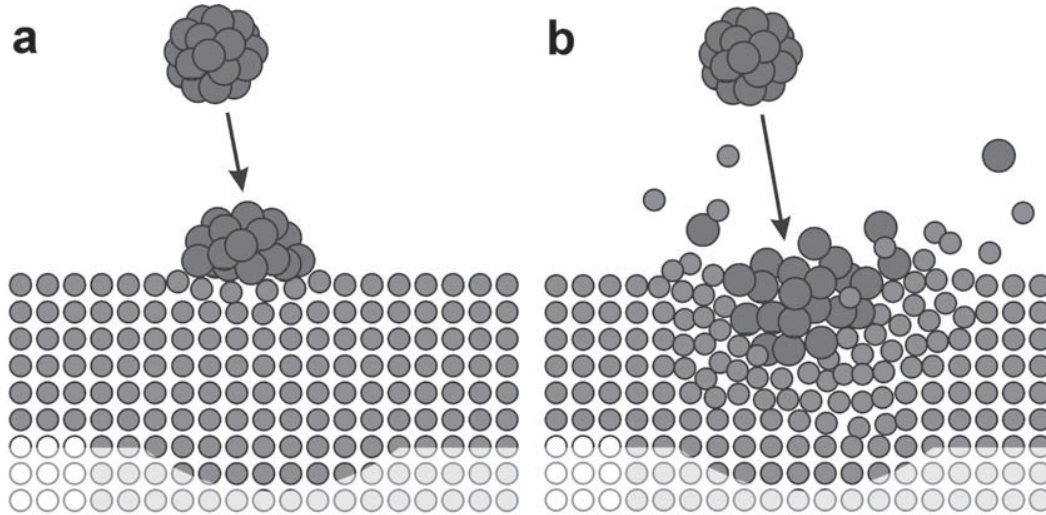


**Figure 2.14.** a schematic representation of a. soft landing and b. energetic impact of clusters [12].

diameter in the time it takes before another cluster would impact a neighbouring position is negligible. If the clusters do not agglomerate or coalesce the morphology is then a random paving of clusters as seen in fig. 2.15. This morphology has been found for e.g. Au clusters on an Au(1 1 1) surface and is stable even when exposed to atmospheric air and room temperature [25]. If there is significant diffusion but no coalescence the morphology consists of large branching islands as seen in fig. 2.16. This morphology can be explained by the numerical deposition diffusion aggregation model. The model proposes that the clusters arrive randomly on the surface with a flux,  $F$ , and then at regular intervals,  $t$ , any isolated clusters move a diameter,  $d$ , in a random direction. It is assumed that when two clusters meet they stick irreversibly together and become stationary. The model predicts a saturated density of islands that is only dependent on the incident flux and the average time,  $\tau$ , it takes for a cluster to move a distance,  $d$ . The diffusion constant,  $D$ , is then by definition:

$$D = \frac{d^2}{4\tau} \quad (2.26)$$

The initial growth of the film is dominated by the nucleation of new islands and as such the average size changes little. Then the growth and nucleation coexist until the number of islands reach saturation. After which growth dominates. The saturation density of islands,  $N$ , is given by:

$$N = 0.41\phi^{0.336} \quad (2.27)$$

Where  $\phi$  is the normalised flux defined as the number of clusters arriving per time,  $\tau$ , per projected cluster area,  $\frac{1}{4}\pi d^2$ , i.e.:

$$\phi = \frac{1}{4}F\tau\pi d^2 \quad (2.28)$$

It should be noted that  $N$  is number of islands per projected cluster area. This direct relationship between  $N$  and  $\phi$  allows for the determination of the diffusion constant simply by counting the number of island per unit area. The growth of these branched structures do not occur if the number of surface defects is too high in which case the random paving morphology is found or is the cluster size is so small that the clusters coalesce as the islands

formed will then be spherical [26].

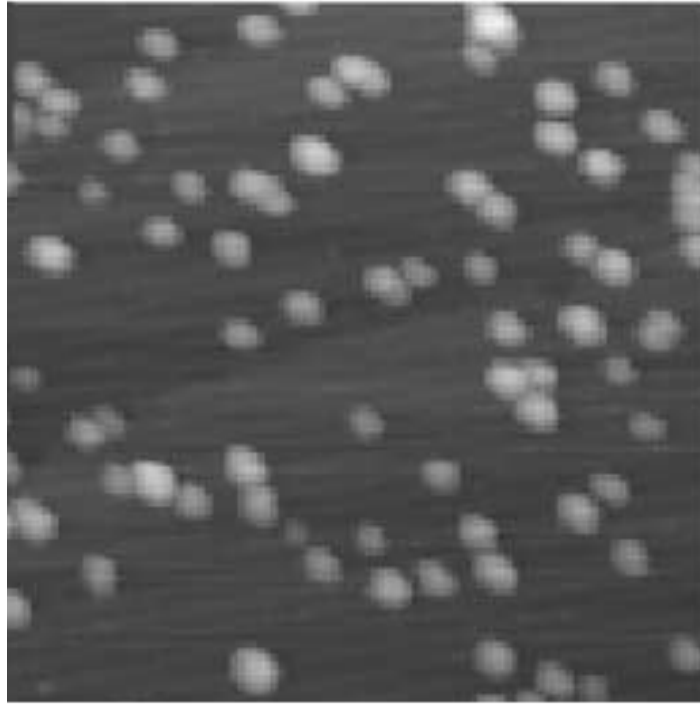


*Figure 2.15.* STM image of Fe clusters on Si(1 1 1) [27].

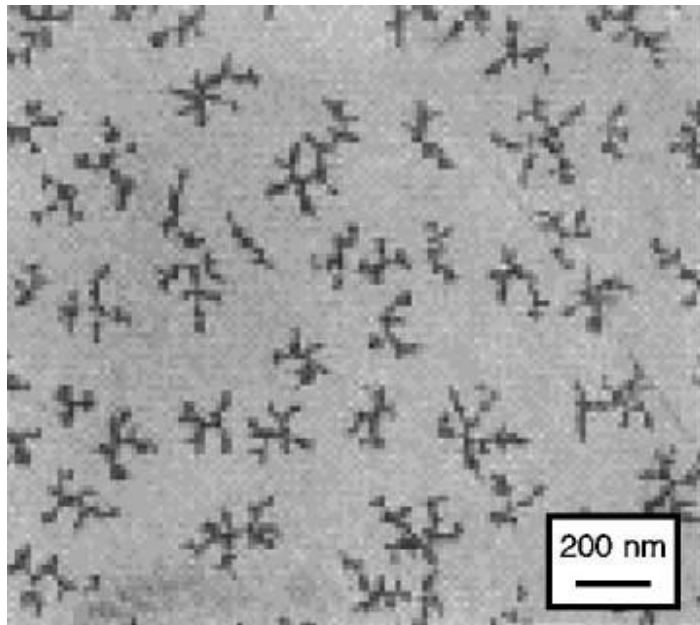


*Figure 2.16.* A TEM image of 2300 atom Sb clusters on graphite [26].

In the regime of high energy impact the cluster will lose its structure as the energy per atom exceeds the binding energy of the cluster see fig. 2.14b. However the cluster will only enter

the surface if the energy is higher than the penetration threshold energy. Below this energy the cluster will either flatten or scatter on the surface. If for example a cluster consisting of Mo impacts a Mo surface with an energy of 1 eV per atom the impact will form a film with a density of up to 80% of the bulk. However if the energy is increased to about 10eV per atom an even denser film with better surface adhesion will form because of intermixing between the deposited atoms and the first few surface layers of the bulk, see fig. 2.17 [28]. High energy deposition also suppresses the surface roughness of the deposited film as the deposited atoms move from the hills and into the valleys of the film.

A boundary case between soft landing and implantation is the regime of pinning where the cluster displaces some surface atoms and implants only part of the cluster. This pinning of the cluster suppresses diffusion of the cluster. These pinned clusters can then be used as immobilization sites for subsequently deposited materials such as organic molecules.

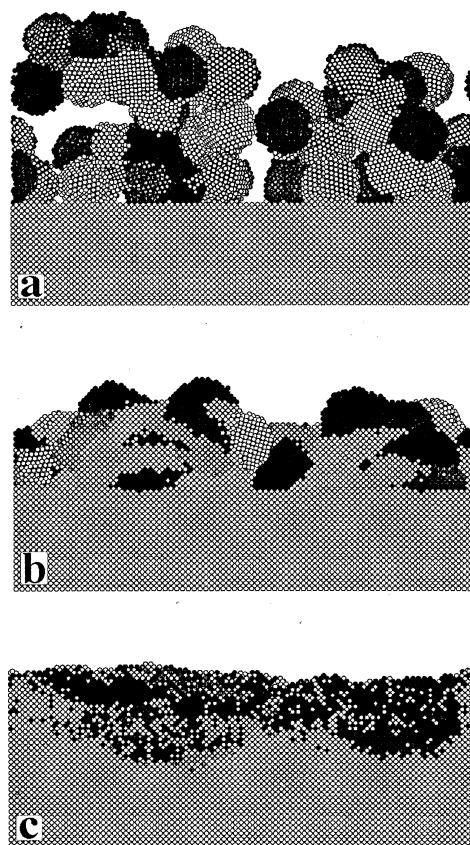


**Figure 2.17.** Simulation of films formed by impact of a Mo cluster with 1043 atoms and a kinetic energy of (a) 0.1eV (b) 1 eV (c) 10 eV per atom.[28]

For clusters the penetration threshold energy per atom is significantly lower than for monomer ions. Due to the weak bonding and large size when compared to monomer ions. Clusters generate multiple collision events. The high density of energy transferred from the cluster to the surface generates conditions that are very similar to a miniature explosion reminiscent of meteor-planet collisions [29]. Molecular dynamics simulation have been used to show that

a cluster rapidly breaks apart, within tens or hundreds of femtoseconds [30]. For clusters having kinetic energies from tens of eV to tens of keV the loss of energy is mostly due to elastic collisions between the atoms. It can therefore be expected that the collision cascades of the cluster atoms will overlap to some degree when they penetrate into the target. Monte Carlo and molecular dynamics simulation have shown that clusters have a greater penetration depth than mono atom deposition at the same velocity.

When an ion of sufficient energy impacts a surface formation of a crater at the impact site may take place, see fig. 2.18. This effect is even more pronounced for clusters where the size of the crater has been found to be dependent on both the size of the cluster and on cluster energy. However a higher energy of the individual cluster constituents leads to a lower rate of crater formation. This is probably related to an increase in the projected range and thereby a shift in the maximum cluster to substrate energy transfer into the sample [12].

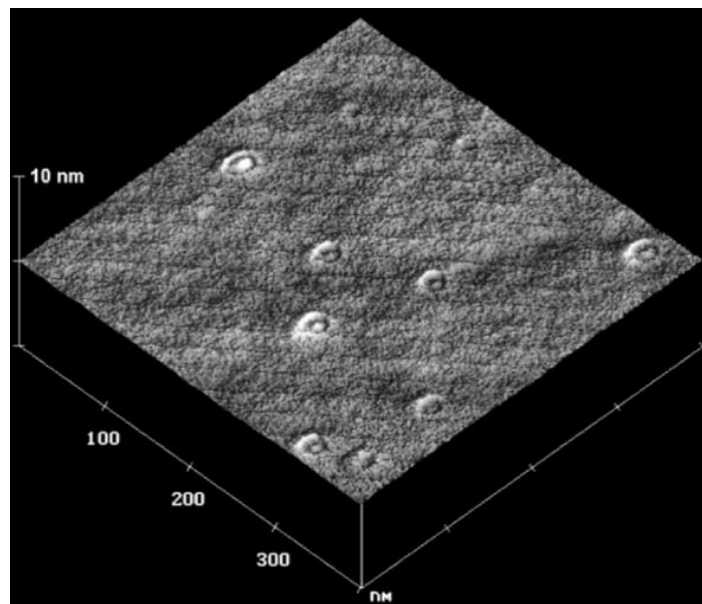


*Figure 2.18.* Craters formed by impact of Ar clusters with 54 atoms and a kinetic energy of 15keV on an Si surface [29].

# Experimental Setup 3

In this chapter the experimental setup and applied methods will be described in detail.

The purpose of the system, see fig. 3.1, is to produce and size select metal clusters. In the current project the clusters are made of copper. All processes involving the production of a sample are done under vacuum. First the copper target is sputtered by plasma and then clusters are nucleated in the aggregation tube where the sputtered material is cooled and appropriate conditions for the cluster formation are provided. Thereafter, the clusters are expelled through the nozzle into the source chamber where the core part of the cloud is collected by the skimmer forming a beam of clusters. This beam then passes through an Einzel lens where the ionic part of the beam is focused and a set of deflectors where the focused beam can be steered vertically or horizontally. The beam then comes to the quadropole mass spectrometer where charged clusters can be size-selected and deflected ninety degrees. The part of the beam that is not deflected will continue straight through and hit a Faraday cup which will measure the current of the beam. The setup is connected to the Cluster Implantation and Deposition Apparatus (CIDA). However, in the testing experiments described in this thesis CIDA was not used. Therefore, its construction is not described. More detail can be found in [31].

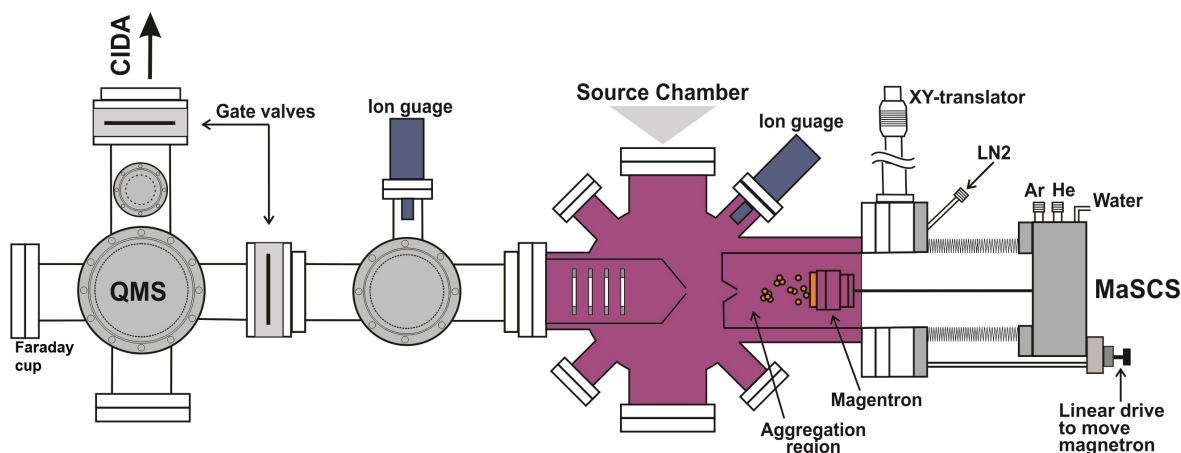
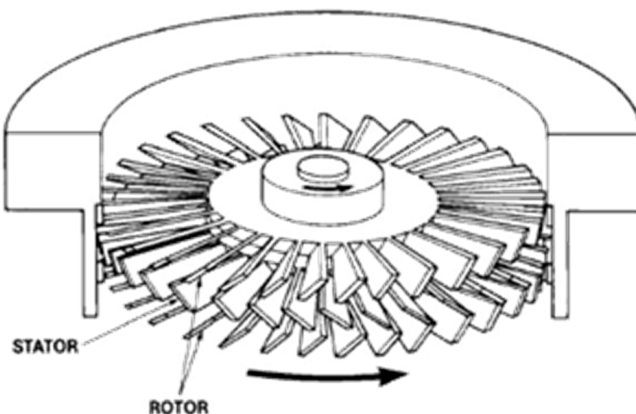


Figure 3.1. A schematic of the setup.

### 3.1 Vacuum Systems

The vacuum system consists of a series of stainless steel chambers that are evacuated by a few pumps. The pumps used are turbomolecular pumps that are backed by rotary-vane pumps. Connections between chambers and the equipment is achieved using conflat, CF, flanges which are then sealed with copper gaskets. Sometimes rubber gaskets are used instead of copper if the flange is intended to be opened frequently for some adjustments inside the chambers.

A turbopump works by having a high-speed rotor that "shuffles" gas atoms from the vacuum side to the backing side where they are pumped away by the backing pump. The rotor turns through and is interleaved with the stator, see fig. 3.2. It has blades that are inclined with respect to the axis of rotation and the stator blade are oppositely inclined. This means that the probability of a molecule passing from the vacuum side to the backing side is a lot higher than the reverse happening this can be seen if one considers the worst case of a molecule going through the pump either way. For a molecule hitting a rotor from the vacuum side at point A, see fig. 3.3 the molecule can go through if it hits with an angle no greater than  $\beta_1$  and leaves within  $\delta_1$ . The same is the case for an atom traveling from the backing side and hitting at point B for the angles  $\beta_2$  and  $\delta_2$  respectively. The probability of an atom going through from either the vacuum or the backing side can be estimated as  $\frac{\delta_1}{\beta_1}$  and  $\frac{\delta_2}{\beta_2}$  respectively. Since  $\frac{\delta_1}{\beta_1}$  is larger than  $\frac{\delta_2}{\beta_2}$  the molecules move from the vacuum to the backing side and pumping occurs [32].



*Figure 3.2.* A schematic representation of a turbomolecular pump. Rotor and stator blades are inclined with respect to one another.

In order for the turbopump to function a backing pump is needed. This function is most often performed by a rotary vane pump, see fig. 3.4. The pump works on the basis of changing gas volumes using an eccentric rotor, with two blades in a diametrical slot. Gas is first taken from the inlet as the volume expands and then as the rotor turns the volume is separated from the inlet and the gas is compressed until it is forced out of the exhaust valve [32].

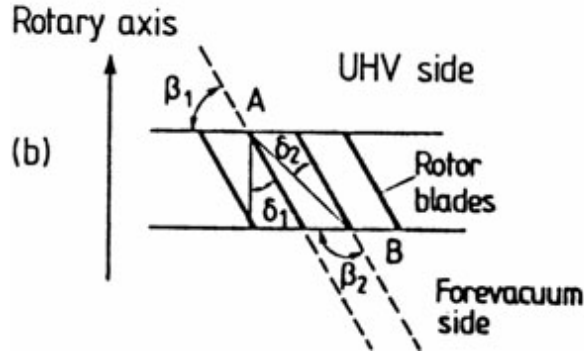


*Figure 3.3.* Qualitative view of the rotor blades. The paths between the vacuum and backing sides are determined by the shown angles [32].

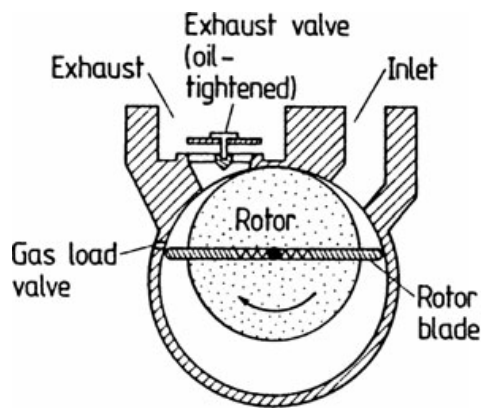


*Figure 3.4.* Schematic representation of a rotary pump [32].

For the setup used in this thesis two turbopumps with backing rotary pumps were used a Pfeiffer vacuum TPH 1201 using a Pentaline 35 as backing pump and a Hipace 400 using a duo line 10 M as backing pump. The turbopumps have a working speed of 630 and 820 Hz respectively.

## 3.2 Magnetron Source

The magnetron source is a commercially available Oxford Applied Research NC200U-B nanocluster source, and can be seen in fig. 3.5. This is a planar magnetron with water cooling behind the target to keep the temperature of the target controlled. The target cathode distance can be adjusted and is for this thesis 0.3 mm. The source has one line for sputtering gas and two lines to supply different carrier gases. For the purposes of this work Ar is used as the sputtering gas and He as the aggregation gas. The source is externally supplied with the required voltage for igniting the plasma. It possesses a linear drive with a range of approximately 100 mm which varies the distance between the sputtering source and the nozzle and thereby varies the path length in the aggregation tube. The aggregation tube is cooled using liquid nitrogen that flows in a tube wrapped around the outside of the aggregation tube.

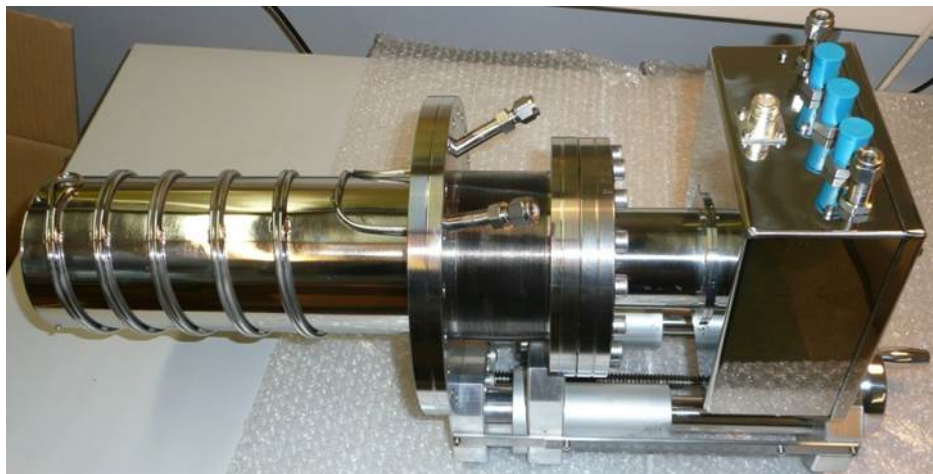


*Figure 3.5.* The magnetron source inserted in the aggregation tube.

The target is a disc of copper with a purity of at least 99.99%. It has a thickness of  $6 \pm 0.5 \text{ mm}$  and a diameter of  $50 \pm 0.5 \text{ mm}$ . The target is mounted on top of a protective disc of Mo, see fig. 3.6.

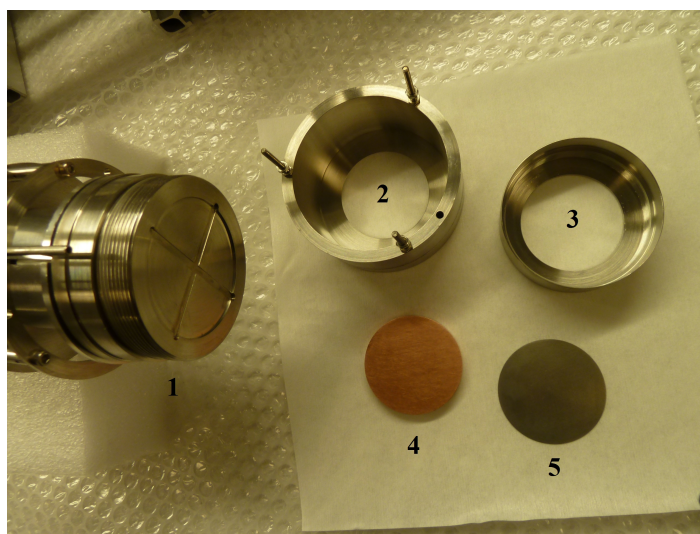


*Figure 3.6.* Disassembled magnetron target holder. Where (1) is the magnetron, (2) is the magnetron cover, (3) is the target holder, (4) is the copper target, and (5) is a protective Mo backplate.

### 3.3 Ion Optics and Quadropole Mass Spectrometer

The ion optics used in the setup, see fig. 3.7, are an Einzel lens, located behind the skimmer, used to focus the beam of clusters and a set of deflectors to control the beam path. The lens consists of three metal plates, the first and third plates are grounded to the chamber whereas the second plate is connected through electrical feedthrough to a power supply located out-

side the vacuum chambers. Voltage applied to the lens can be adjusted from 0 to 3 kV. Next are two sets of deflector plates which can be used to change the direction of the beam each set has one plate that is grounded to the chamber and one electrically to an external power supply to adjust applied voltage, thus, to control deflection of the beam. One set can deflect the beam in horizontal direction and the other one in vertical.

The next active component the beam will encounter is the electrostatic quadropole mass

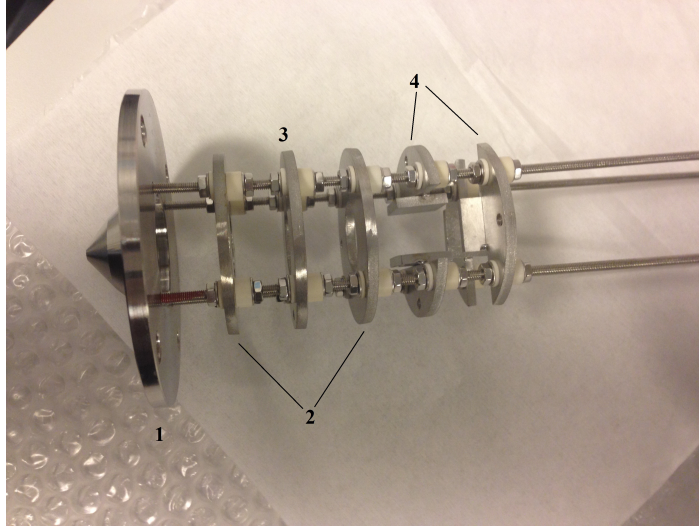


**Figure 3.7.** The ion optics positioned after the aggregation chamber. (1) The skimmer, (2) The grounded Einzel lens plates, (3) the biased Einzel lens plate, and (4) the deflectors.

spectrometer (QMS) which consists of four quarter cylindrical electrodes which are under positive potential on one diagonal and a negative one on the other, see fig. 3.8. These electrodes are surrounded by a grounded shield which has circular orifices of 10 mm for the beam to pass through, see fig. 3.9.

If one approximates the electrodes as hyperbolic then the voltage applied to the electrodes,  $U_{QP}$ , will create an electrical field with hyperbolic equipotential lines. Thus a particle with a kinetic energy,  $E_k = \frac{1}{2}mv^2$  where  $m$  is its mass and  $v$  its velocity, equal to the pass energy of the quadropole:

$$E = qU_{QP}, \quad (3.1)$$

where  $q$  is the charge of the particle. Will experience the required 90 degree turn and leave through the exit aperture, see fig. 3.8. Therefore the mass to charge ratio selected will be:

$$\frac{m}{q} = \frac{2 \cdot U_{QP}}{v^2}. \quad (3.2)$$

If one assumes that the particles all have the same charge and the same velocity the cluster can be perfectly mass selected by changing the applied voltage. This scenario assumes a perfectly collimated beam adjusted exactly along the main axes. In practice one will have to account for beam divergence, velocity dispersion, velocity slippage and possible multi charged clusters. These effects all lead to a broadening of the kinetic energy which will affect the mass selection. Furthermore the electrodes of the QMS used in this work are not perfectly

hyperbolic. Which necessitates a geometric correction factor which is usually in the range of 1.5-2 this factor can be either simulated or experimentally determined [20].

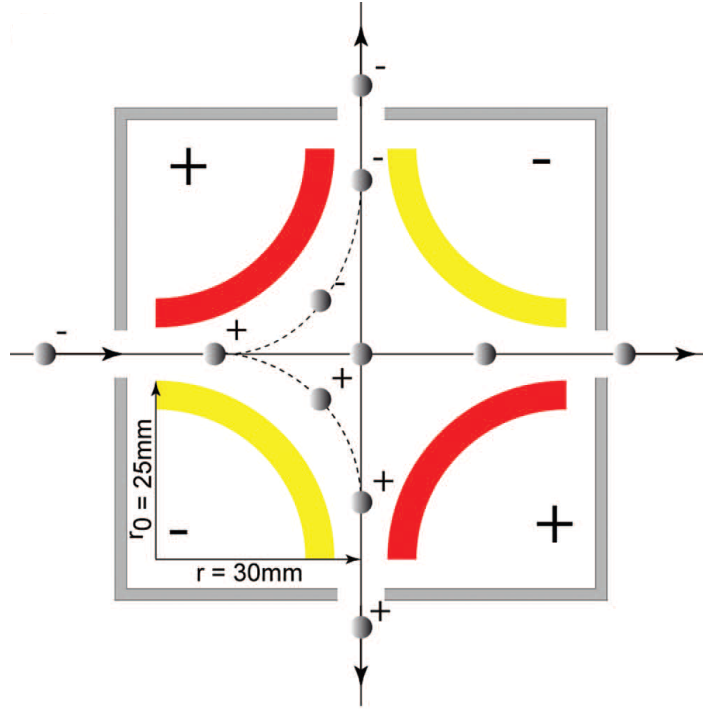


*Figure 3.8.* A schematic representation of the beam path through a QMS [20].

### 3.4 Characterization of deposited clusters by AFM

Once clusters are deposited on a sample they can have their topography imaged using an atomic force microscope (AFM). As can be seen in fig. 3.10 an AFM consists of a micro-machined cantilever probe with a sharp tip mounted on a piezoelectric actuator as well as a position sensitive photo detector for detecting the laser reflected off the endpoint of the cantilever to provide feedback on the cantilever deflection. This is due to the path of the laser being changed when the reflector on the backside of the cantilever changes its angle as the cantilever is deflected. This is picked up by a multi cell photo detector as the signal from each cell changes when the laser no longer hits each equally. The basic principle of operation is to scan the tip over the sample surface and using the feedback mechanisms to have the piezo actuator maintain either a constant force or a constant height above the surface. There are three main modes of operation as can be seen on fig. 3.11. Contact mode where the tip is in constant contact with the surface as it scans, semi-contact or tapping mode where the tip is in intermittent contact with the surface, and the noncontact mode where the tip oscillates above the surface.

For the purposes of this work semi-contact mode was used, which means that the cantilever oscillates with an amplitude on the nanometre scale in close vicinity to the surface, making intermittent contact, and the attractive Van der Waals forces between the tip and the sample are measured. These forces are however, so small that it becomes necessary for

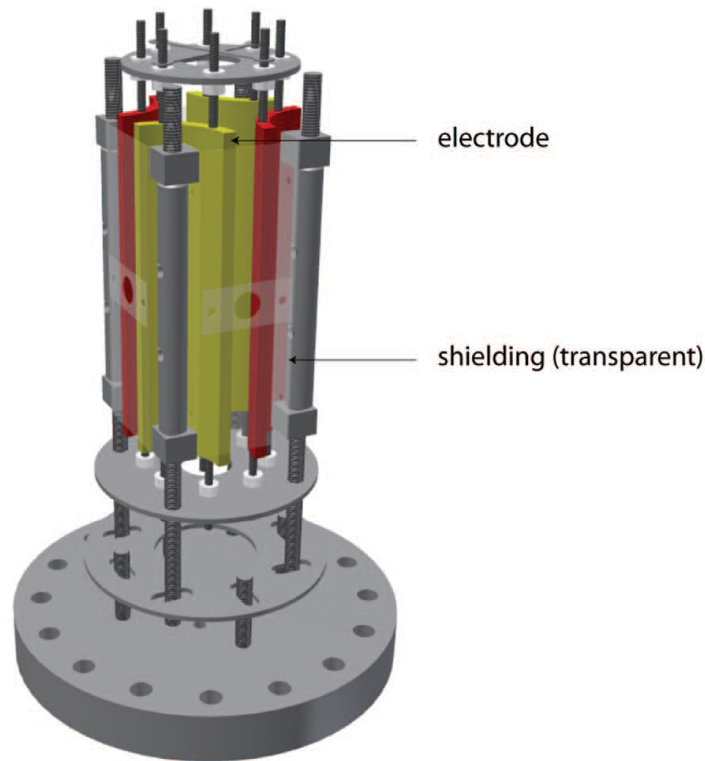


*Figure 3.9.* Pseudo 3D view of the quadropole [20].

the cantilever to oscillate at or near its resonance frequency in order to detect the shift in amplitude, phase, and frequency caused by the attractive forces. Usually the topography is imaged using the shift in amplitude caused when the tip is in the Van der Waals regime. An advantage of the semi-contact mode compared to the contact mode, see fig. 3.11, where the tip is dragged across the surface, is the smaller amount of damage caused to both the tip and the sample. Another is the relatively small forces between the tip and the sample which for the case of clusters reduces the risk of the tip moving the clusters about on the sample [33].

In this work an Ntegra atomic force microscope, manufactured by NT-MDT, was employed in semi-contact mode. Commercial silicon cantilevers with tip curvature radii below 10 nm were used.

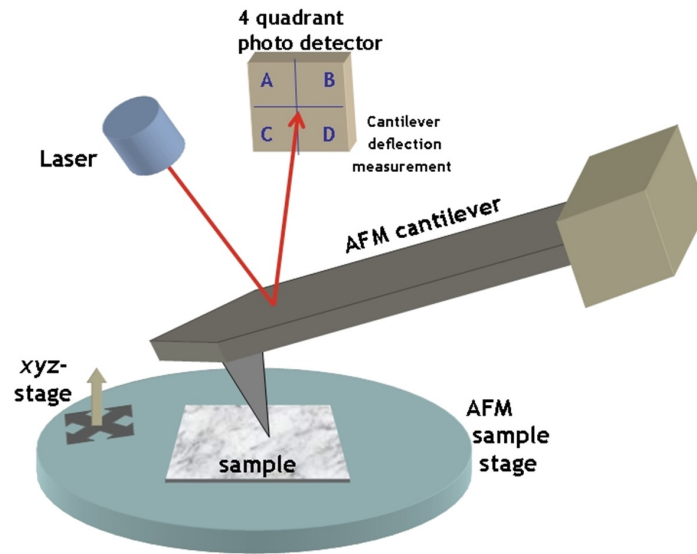


Figure 3.10. Illustration of the principal workings of an AFM.

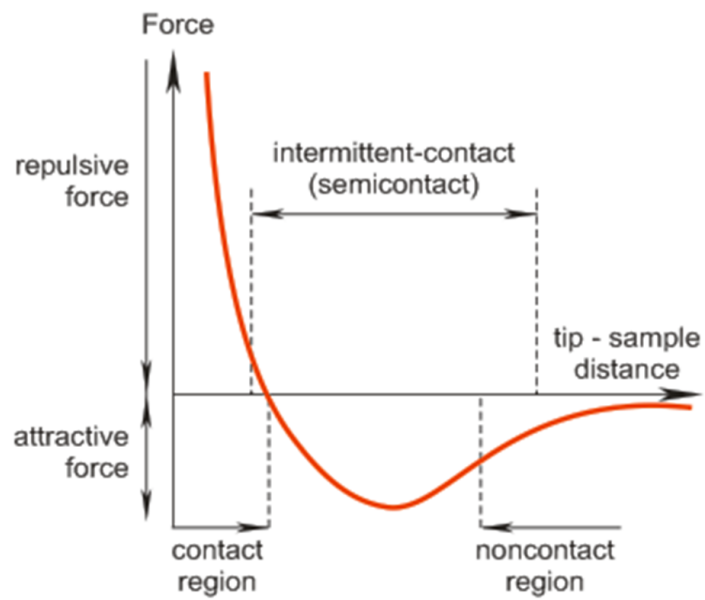


Figure 3.11. Interatomic force variance by distance.

# Optimization of the Magnetron Cluster Source

# 4

---

In this chapter the steps taken to optimise and calibrate the setup are described starting with the procedure for optimising the Einzel lens and deflector voltages. Deposition was performed on different substrates followed by experiments to determine the parameters for size selection using different electrostatic quadrupole mass spectrometer voltages.

## 4.1 Optimizing lens and deflector voltages

In order to find the optimal parameters for size selection and deposition of the clusters first the main axis had to be aligned. This was done first with a spirit level and then by shining a diverging light source through the central axis. Once this was done the voltages applied to the ion optics had to be optimized this was done using a round plate on manipulator mounted instead of the second ion gauge. The cluster beam was initialized and measured with the Faraday cup. Then the desired voltage was applied to the Einzel lens and the deflectors after which the beam was allowed to stabilize. The plate was then inserted into the path of the beam using the manipulator. The plate was left in the beam for an amount of time, see table 4.1, after which it was removed and the beam turned off. The spot of deposited clusters on each plate, see fig. 4.1, was then examined to determine the viability of the applied voltage. It was observed that even when the beam was very tightly focused that the spot was not circular but seemed elongated which was suspected to be caused by the circular spot being partially blocked. It was discovered to have been caused by a slight misalignment of the nozzle and skimmer which was corrected before sample 8 was made. This then led to the circular or nearly circular spots found on the last samples.

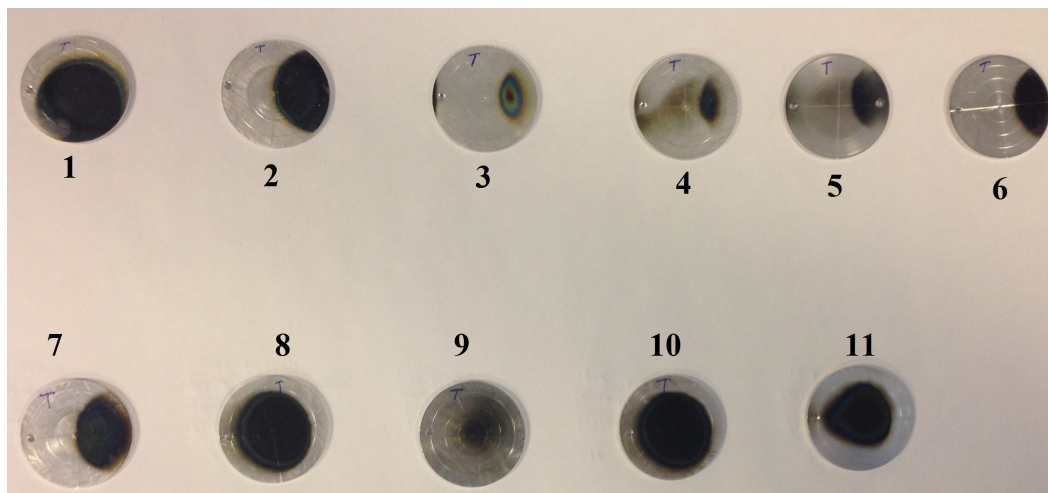


**Figure 4.1.** Metal plates with clusters deposited used for alignment of main axis and optimization of ion optics voltages. See table 4.1 for parameters.

## 4.2 Testing of the Quadropole Mass Spectrometer

The static parameters for the later experiments were found by measuring the current of the cluster beam entering Faraday cup (see Fig. 3.1). The parameters were tuned to maximize the current. After that the QMS voltage was turned on and the ion optics voltages were changed until a maximum in current was reached. In this case the current was measured using a second Faraday cup on the flange located on QMS under 90 degrees with respect to the main axis of the setup. In the table below, the static parameters for the experiments are listed. Some such as the sputter current and the gas flows come from the manual for the magnetron source where the others come from the optimization of the signal at the Faraday cup after the mass selection. The final static parameters for deposition are given in in table 4.2.

**Table 4.1.** Parameters for the experiments performed to optimise the lens and deflector voltage.

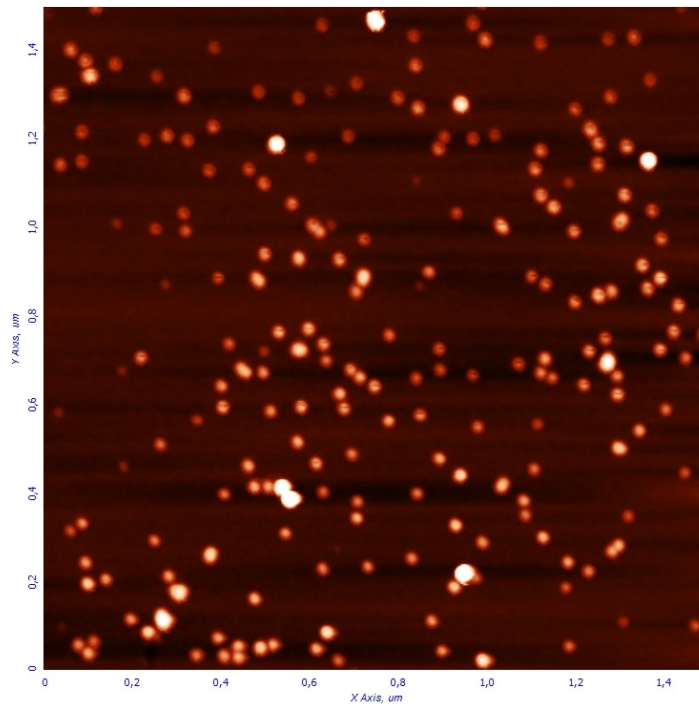
Sample Number	Lens Voltage [V]	Deflector Voltage [V]	Deposition Time [minutes]	Notes
1	0	0	56	
2	150	0	20	
3	100	0	10	
4	100	40	12	
5	100	-40	12	
6	-100	0	20	
7	0	0	20	
8	0	0	12	Skimmer and nozzle realigned
9	-100	0	12	
10	100	0	12	
11	-315	0	12	

**Table 4.2.** Static parameters for the subsequent experiments.

Source extension	100 mm
Sputter current	200 mA
Ar flow	50 sccm
He flow	9 sccm
Lens voltage	+225 V
Vertical deflector voltage	0 V
Horizontal deflector voltage	- 21 V

#### 4.2.1 Cluster Deposition on Different Substrates

First clusters were deposited on three different substrates to determine which would be used in the size selection experiments. The substrates were mica, Highly Ordered Pyrolytic Graphite (HOPG), and Silicon (n-type (100) surface exposed). In figures 4.2, 4.4, and 4.8 AFM images can be seen of the different samples prepared with a quadrupole voltage of  $\pm 400$  V. Before deposition the mica and HOPG samples were exfoliated and the Si sample was cleaned using ethanol.

**Figure 4.2.** AFM image of clusters deposited on mica at QMS voltage of  $\pm 400$  V

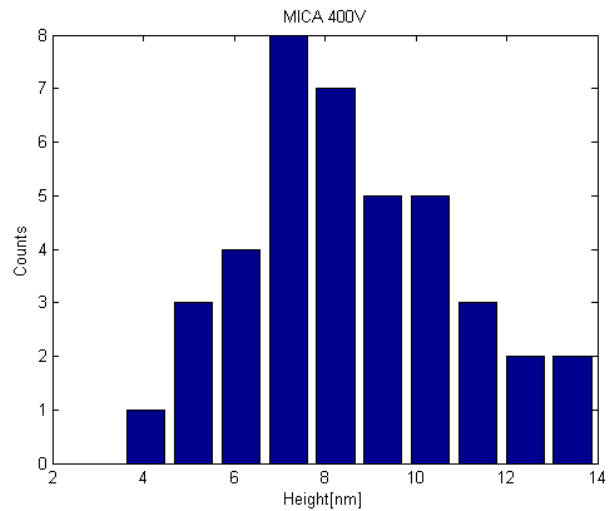


**Figure 4.3.** Histogram of the height of the clusters measured on fig 4.2 with a mean value of 8.6 nm and a standard deviation of 2.4 nm

The mica sample, see fig 4.2 for the AFM image and fig 4.3, had macroscopic cracks and showed a tendency towards charging as the sample was scanned in the AFM which would periodically deteriorate the image quality beyond use.

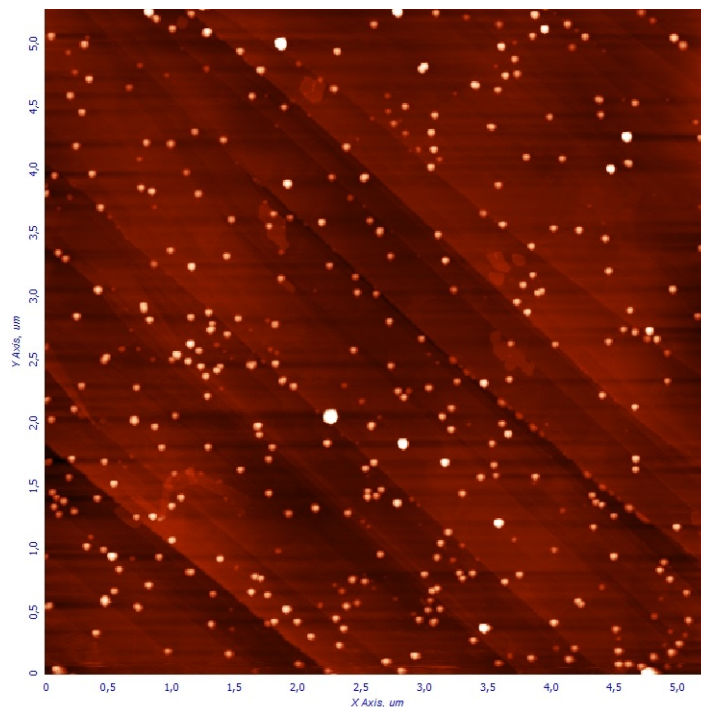


**Figure 4.4.** AFM image of clusters deposited on HOPG at QMS voltage of  $\pm 400$  V

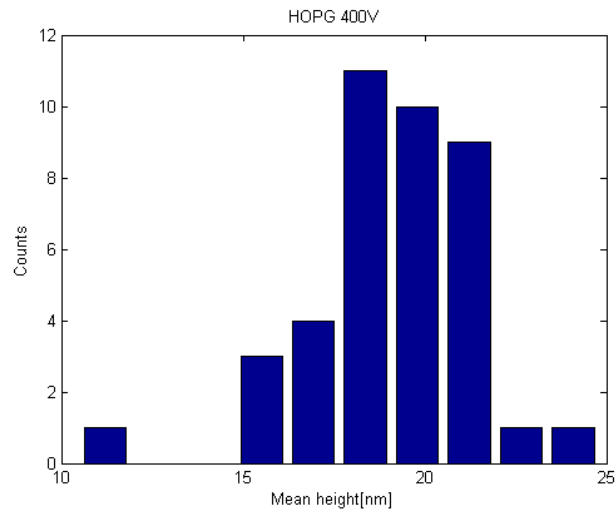


**Figure 4.5.** Histogram of the height of the clusters measured on fig 4.4 with a mean value of 19.1 nm and a standard deviation of 2.4 nm

As can be seen from both fig 4.4 and fig 4.5 the cluster size appeared to be much larger than the one observed for the other samples. To ascertain whether this was caused by a momentary instability of the cluster source or a more general tendency for HOPG a second sample was produced.

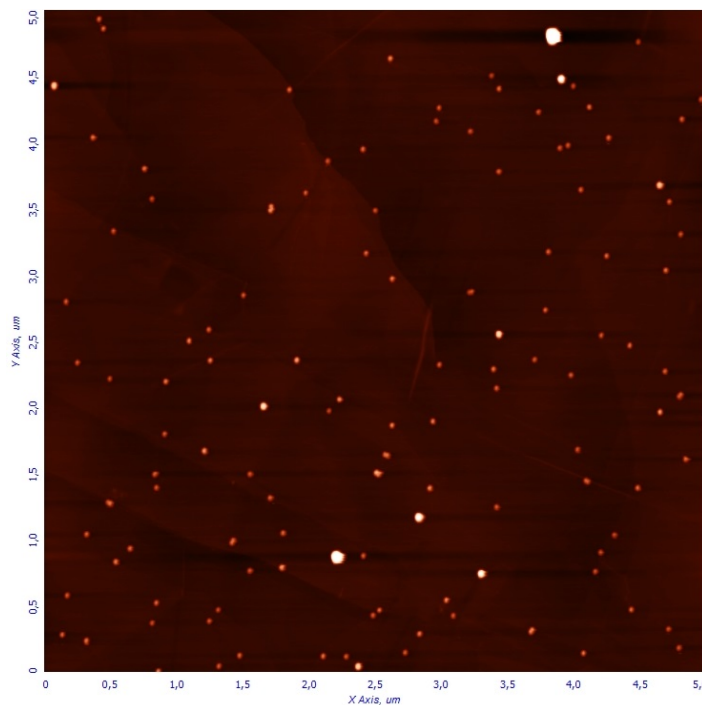


**Figure 4.6.** AFM image of the second sample with clusters deposited on HOPG at QMS voltage of  $\pm 400$  V

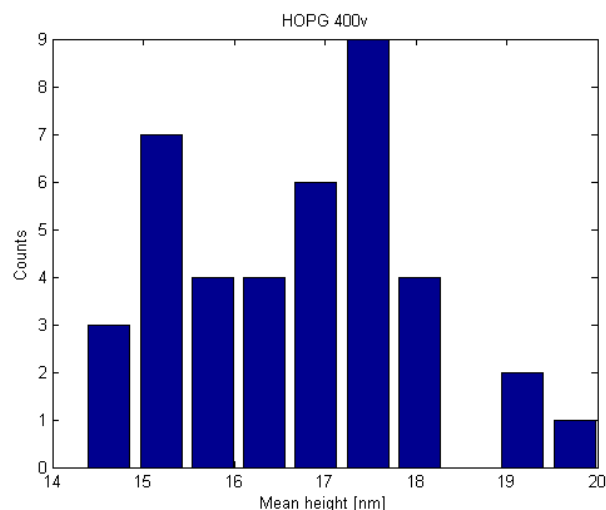


*Figure 4.7.* Histogram of the height of the clusters measured on fig 4.4 with a mean value of 16.7 nm and a standard deviation of 1.3 nm

In figs 4.6 and 4.7 can be seen an AFM image and corresponding size histogram for the second graphite sample. As is immediately apparent the mean size is still well above that of the silicon and mica samples which indicates that the cluster were not deposited at this size. In [34] it was observed that small clusters of silver deposited on HOPG diffused rapidly until they formed island with a mean height of 14 nm. This size was theorized to be determined by the strain between the HOPG surface and the silver lattice. An analogy to this could be what causes the larger observed cluster, or more precisely island, size. The high mobility of the clusters on the surface was also directly observed when imaging the sample as the tip would move the clusters on the surface while scanning. This problem could be alleviated by increasing the setpoint and thereby decreasing the force between the tip and the clusters.

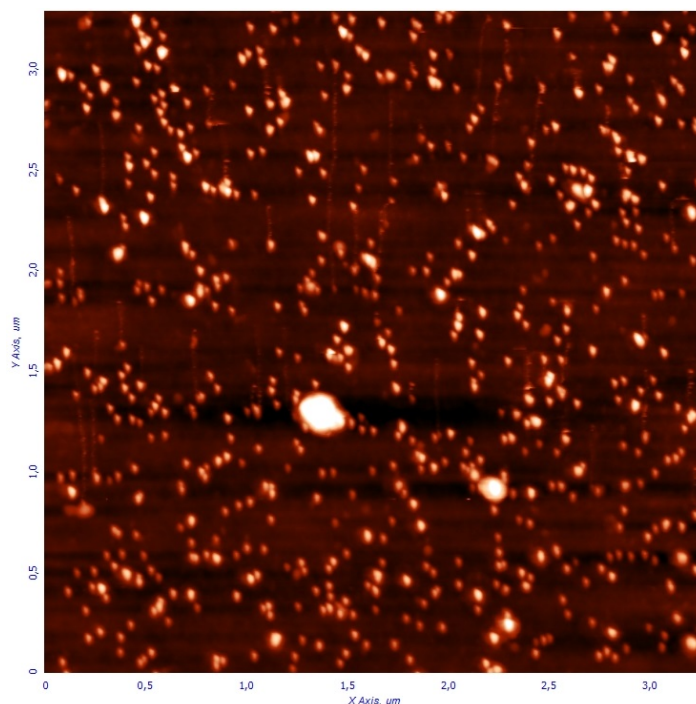


**Figure 4.8.** AFM image of clusters deposited on Si at QMS voltage of  $\pm 400$  V

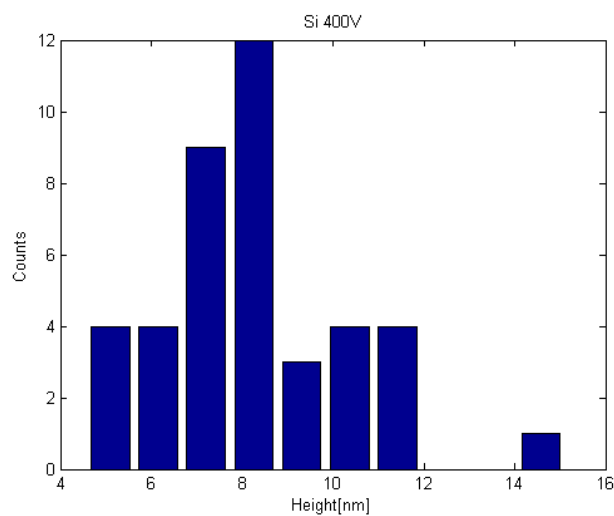


**Figure 4.9.** Histogram of the height of the clusters measured on fig 4.8 with a mean value of 8.3 nm and a standard deviation of 2.1 nm

Lastly the silicon surface, see fig 4.8 and fig 4.9, shows neither the tendency towards charging as the mica nor the non-random paving shown by the HOPG. The random paving observed is due to the low diffusivity of the clusters on the surface which is likely caused by the roughness of the silicon. However it did like the HOPG sample experience some movement of the clusters on the surface when the force between the AFM tip and the clusters was too high, seen as vertical stripes on the AFM image.

Silicon was chosen as the substrate both due to the roughness of the surface which caused less diffusion and due to the absence of large-scale surface defects such as atomic steps which also contributed to a random paving of the sample. The random paving along with the current rate of coverage simplified the identification of each individual cluster height. This is necessary for accurately determining the size selection as once layers of clusters begin to form the individual height becomes difficult to determine and once one or more complete monolayers have formed the height can no longer be accurately determined. As there will be no clearly defined surface. Mica was not chosen as a substrate due to the charging observed when the sample was scanned in the AFM. Neither was HOPG due to the high diffusivity on the surface which caused coalescence of the clusters. On HOPG the clusters also had a tendency towards aggregating at atomic steps.

#### 4.2.2 Size Selection

The next step was to obtain the size distribution of several other quadropole voltages which was done at 100 V (figs 4.10, 4.11), 500 V (figs 4.12, 4.13), and 100 V (figs 4.14, 4.15). For height measurements some very large aggregates of clusters were disregarded.

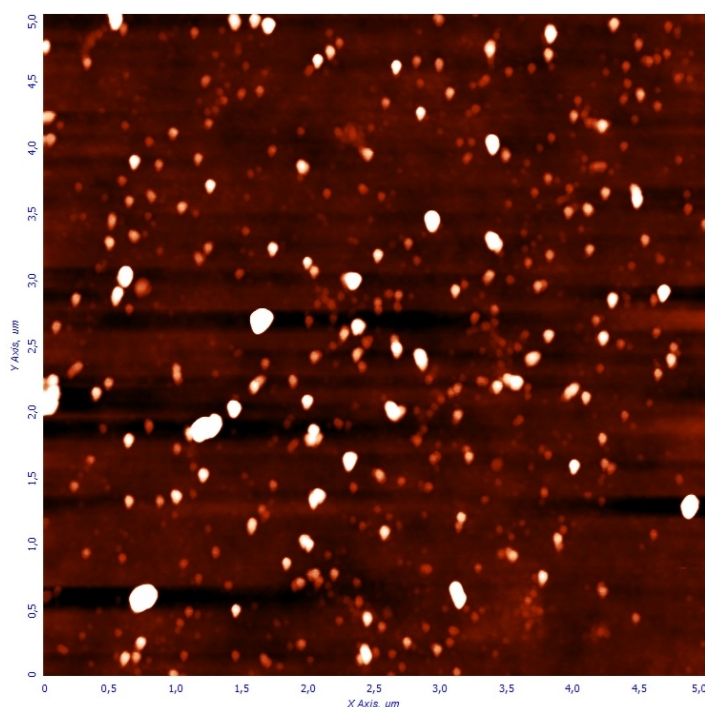


*Figure 4.10.* AFM image of clusters deposited on Si at QMS voltage of  $\pm 100$  V

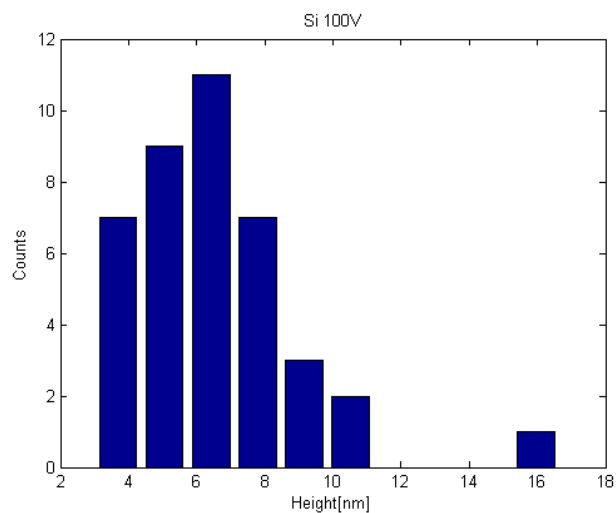


*Figure 4.11.* Histogram of the height of the clusters measured on fig 4.10 with a mean value of 6.5 nm and a standard deviation of 2.5 nm

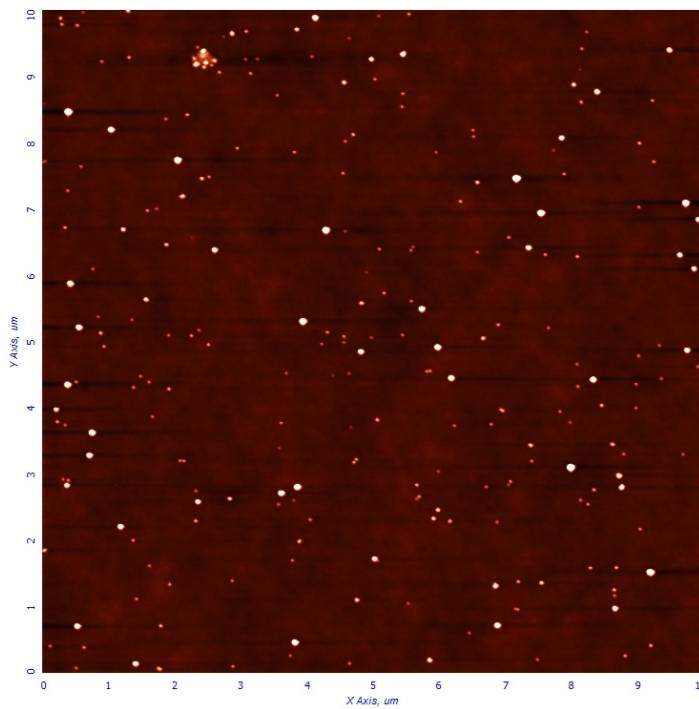


*Figure 4.12.* AFM image of clusters deposited on Si at QMS voltage of  $\pm 500$  V

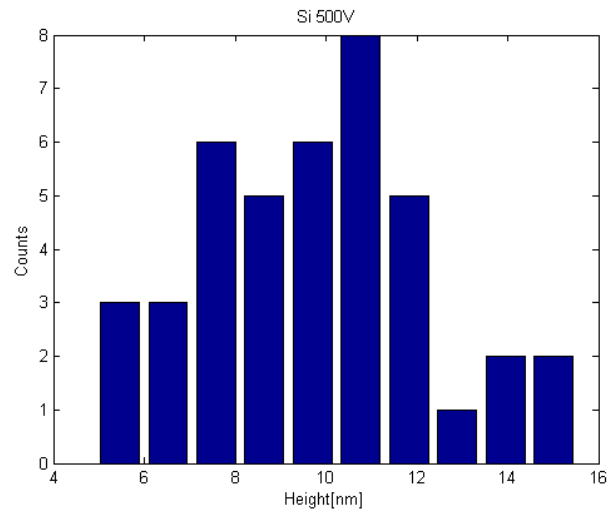


*Figure 4.13.* Histogram of the height of the clusters measured on fig 4.12 with a mean value of 9.7 nm and a standard deviation of 2.5 nm

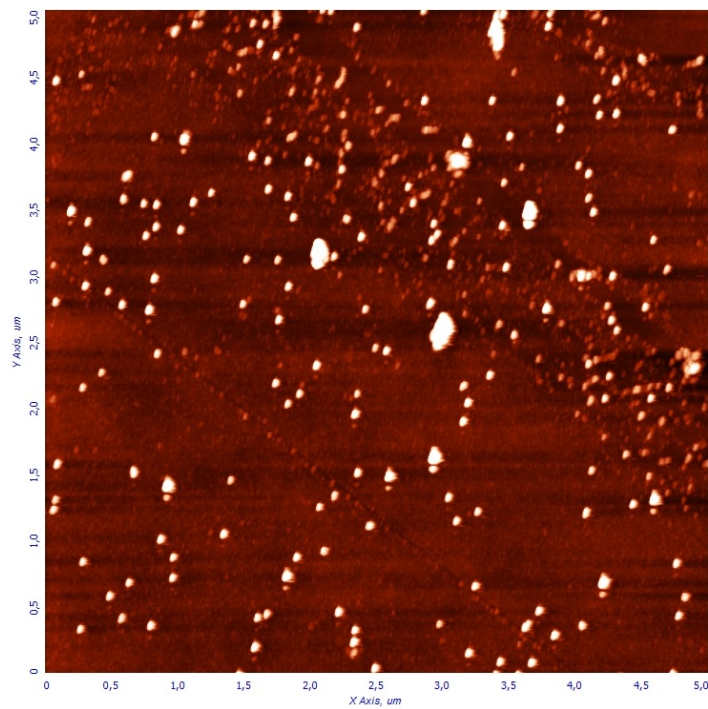


*Figure 4.14.* AFM image of clusters deposited on Si at QMS voltage of  $\pm 1000$  V

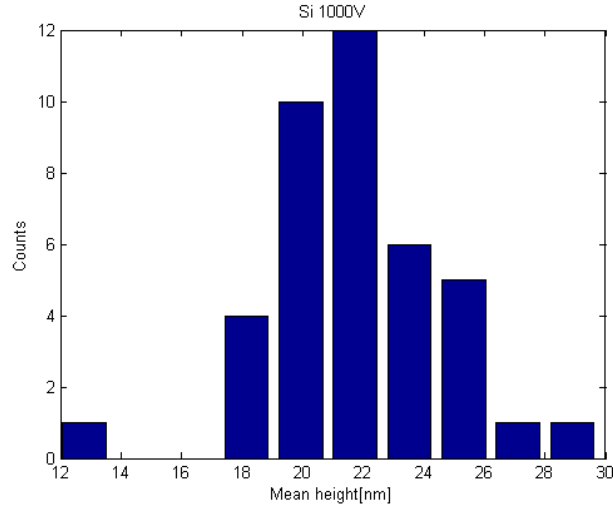


**Figure 4.15.** Histogram of the height of the clusters measured on fig 4.14 with a mean value of 21.8 nm and a standard deviation of 3 nm

The expected dependence between the applied QMS voltage and the height of the deposited clusters will, assuming that the velocity distribution and charge of the clusters are independent of the mass. As well as the height of the deposited clusters being linearly proportional to the cluster radius in the beam. Will be a cube root proportionality that is:

$$U_{qp} \propto m_c \propto r_c^3 \quad (4.1)$$

$$r_c \propto \sqrt[3]{U_{qp}}, \quad (4.2)$$

where  $U_{qp}$  is the voltage applied to the QMS,  $m_c$  is the mass of the cluster, and  $r_c$  is the radius of the cluster. This means that it would be expected larger clusters when larger voltages are applied and that this increase will taper off at some point.

The experimental results are in agreement with the dependence given in equation 4.1. The increase in cluster height with increasing applied QMS voltage can be seen both in fig. 4.16 and in table 4.3. While some coalescence have been observed on several samples this is almost completely unavoidable as the clusters will be able to diffuse short distances unless they are pinned to or implanted in the substrate.

**Table 4.3.** Mean and standard deviation for the measured heights.

Sample material	Quadropole voltage [V]	Mean height [nm]	Standard deviation [nm]
Si	100	6.46	2.52
Si	400	8.25	2.05
Si	500	9.74	2.51
Si	1000	21.80	2.96

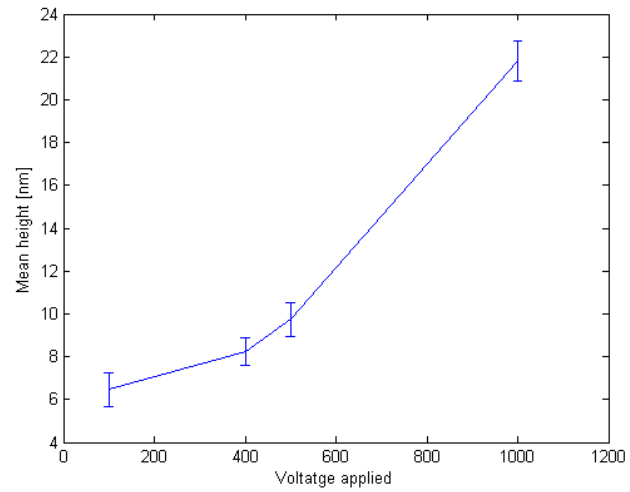


*Figure 4.16.* Plot of voltage versus mean height with error bars representing 95% confidence interval.

# Conclusion 5

---

The goal of the project described in this thesis was to construct and test a setup for production and size selection of metal clusters using a magnetron sputtering source and an electrostatic quadropole mass spectrometer respectively. With this goal in mind some theory describing metal clusters and the production and deposition of these has been presented along with a description of the constructed setup and the most central of its components.

Three sets of experiments were performed. The first was done by depositing the non size selected beam onto round plates of aluminium to determine focusing voltages and alignment of the nozzle and skimmer. A lens voltage of -315 V was found to give the best centred and most circular spot on the aluminium plate. This was then followed by optimizing the ion optics parameters using the signal from two faraday cups one measuring the non size selected cluster beam and one measuring the size selected beam. The new deposition parameters for focusing positively charged clusters were a horizontal deflector voltage of -21 V and a lens voltage of +225 V.

The second set of experiments was performed on three different substrate materials (mica, HOPG, and Si) at the same deposition parameters given in table 4.2 and a QMS voltage of  $\pm 400$  V. The AFM study shows that clusters deposited on silicon substrate are stable and randomly paved on the surface. While the mica sample showed the expected size distribution a tendency towards charging made it a less than optimal choice. Highly ordered pyrolytic graphite was another possibility but due to its atomic flatness the clusters rapidly diffused and coalesced, The clusters also showed a tendency towards aggregating at atomic steps on the surface.

The third set of experiments was conducted to test the size selection at different electrostatic quadropole mass spectrometer voltage (100, 400, 500, and 1000 V) on the same substrate material (Si) using the parameters given in table 4.2. The height analysis of AFM images show that cluster size increases with increasing QMS voltage which is in agreement with the theoretical prediction.

# Bibliography

---

- [1] Roy L. Johnston. *Atomic and Molecular Clusters*. Master's Series in Physics and Astronomy. Taylor and Francis, London, 2002.
- [2] R.S. Berry and H. Haberland. Introduction. In Hellmut Haberland, editor, *Clusters of Atoms and Molecules: Theory, Experiment, and Clusters of Atoms*. Springer-Verlag, Berlin, 1994.
- [3] Vladimir N. Popok, Ingo Barke, Eleanor E.B. Campbell, and Karl-Heinz Meiwes-Broer. Cluster-surface interaction: From soft landing to implantation. *Surface Science Reports*, 66:347, 2011.
- [4] Noriaki Toyoda and Isao Yamada. Gas cluster ion beam equipment and applications for surface processing. *IEEE Transactions ON Plasma Science*, 36:1471, 2008.
- [5] Julio A. Alonso. *Structure and Properties of Atomic Nanoclusters*. Imperial College Press, 2005.
- [6] Bernd von Issendorff and Ori Cheshnovsky. Metal to insulator transition in clusters. *Annu. Rev. Phys. Chem.*, 56:549, 2005.
- [7] Puru Jena and Jr. A. W. Castleman. Clusters: A bridge across the disciplines of physics and chemistry. *Proceedings of the National Academy of Sciences of the United States of America*, 103(28):10560–10569, 2006.
- [8] W.D. Knight, Walt A. De Heer, Winston A. Saunders, Keith Clemenger, M.Y. Chou, and Marvin L. Cohen. Alkali metal clusters and the jellium model. *Chemical Physics Letters*, 134(1):1 – 5, 1987.
- [9] John A. Blackman. Shell models of isolated clusters. In John A. Blackman, editor, *Handbook of Metal Physics*, volume 5: Metallic Nanoparticles. Elsevier, Amsterdam, 2008.
- [10] Hellmut Haberland, Thomas Hippler, Jörn Donges, Oleg Kostko, Martin Schmidt, and Bernd von Issendorff. Melting of sodium clusters: Where do the magic numbers come from? *Physical Review Letters*, 94, 2005.
- [11] T. P. Martin. Shells of atoms. *Physics Reports*, 273:199–241, 1996.
- [12] V. N. Popok and E. E. B. Campbell. Beams of atomic clusters: Effects on impact with solids. *Rev. Adv. Mater. Sci.*, 11:19–45, 2006.

- [13] H. Haberland. Experimental methods. In Hellmut Haberland, editor, *Clusters of Atoms and Molecules: Theory, Experiment, and Clusters of Atoms*. Springer-Verlag, Berlin, 1994.
- [14] C. Binns. Production of nanoparticles on supports using gas-phase deposition and mbe. In John A. Blackman, editor, *Handbook of Metal Physics*, volume 5: Metallic Nanoparticles. Elsevier, Amsterdam, 2008.
- [15] P.J Kelly and R.D Arnell. Magnetron sputtering: a review of recent developments and applications. *Vacuum*, 56(3):159 – 172, 2000.
- [16] Jhon A. Thornton. Magnetron sputtering: basic physics and application to cylindrical magnetrons. *Journal of Vacuum Science and Technology*, 171(15), 1978.
- [17] Klaus Ellmer. Magnetron sputtering of transparent conductive zinc oxide: relation between the sputtering parameters and the electronic properties. *J. Phys. D: Appl. Phys.*, 33:R17–R32, 2000.
- [18] Stephen M. Rossnagel. Magnetron plasma deposition process. *Thin Solid Films*, 171:125–142, 1989.
- [19] T A van der Straaten, N F Cramer, I S Falconer, and B W James. The cylindrical dc magnetron discharge: I. particle-in-cell simulation. *J. Phys. D: Appl. Phys.*, 31:177, 1998.
- [20] H. Hartmann, V. N. Popok, I. Barke, V. von Oeynhausen, and K.-H. Meiwes-Broer. Design and capabilities of an experimental setup based on magnetron sputtering for formation and deposition of size-selected metal clusters on ultra-clean surfaces. *Rev. Sci. Instrum.*, 83, 2012.
- [21] P. Milani and S. Iannotta. *Cluster Beam Synthesis of Nanostructured Materials*. Springer-Verlag, 1999.
- [22] David R. Miller. Free jet sources. In Giancinto Scoles, editor, *Atomic and Molecular Beam Methods*, volume 1. Oxford University Press, Oxford, 1988.
- [23] Hermann Wollnik. Ion optics in mass spectrometers. *Journal Of Mass Spectrometry*, 34:991–1006, 1999.
- [24] Walt A. de Heer. The physics of simple metal clusters: experimental aspects and simple models. *Reviews of Modern Physics*, 65:611–676, 1993.
- [25] L. Bardotti, B. Prével, P. Mélinon, A. Perez, Q. Hou, and M. Hou. Deposition of  $\text{Au}_N$  clusters on  $\text{Au}(111)$  surfaces. ii. experimental results and comparison with simulations. *Phys. Rev. B*, 62:2835–2842, 2000.
- [26] C. Binns. Nanoclusters deposited on surfaces. *Surface Science Reports*, 44:1 – 49, 2001.
- [27] M. D. Upward, B. N. Cotier, P. Moriarty, P. H. Beton, S. H. Baker, C. Binns, and K. Edmonds. Deposition of Fe clusters on Si surfaces. *Journal of Vacuum Science and Technology B*, 18:2646, 2000.

- [28] Hellmut Haberland, Zinetulla Insepov, and Michael Moseler. Molecular-dynamics simulation of thin-film growth by energetic cluster impact. *Physical Review B*, 51:11061, 1995.
- [29] V.N. Popok, S.V. Prasalovich, and E.E.B. Campbell. Surface nanostructuring by implantation of cluster ions. *Vacuum*, 76:265–272, 2004.
- [30] Juha Samela and Kai Nordlund. Atomistic simulation of the transition from atomistic to macroscopic cratering. *Physical Review Letters*, 101:027601, 2008.
- [31] V. N. Popok, S. V. Prasalovich, M. Samuelsson, and E. E. B. Campbell. Design and capabilities of a cluster implantation and deposition apparatus: First results on hillock formation under energetic cluster ion bombardment. *Review of Scientific Instruments*, 73:4283–4287, 2002.
- [32] Hans Lüth. *Solid Surfaces, Interfaces and Thin Films*. Springer-Verlag, 2010.
- [33] Nader Jalili and Karthik Laxminarayana. A review of atomic force microscopy imaging systems: application to molecular metrology and biological sciences. *Mechatronics*, 14:907–945, 2004.
- [34] I. M. Goldby, L. Kuipers, B. von Issendorff, and R. E. Palmer. Diffusion and aggregation of sizeselcted silver clusters on a graphite surface. *Applied Physics Letters*, 69:2819, 1996.